HHS Public Access

Author manuscript

Nat Neurosci. Author manuscript; available in PMC 2021 February 20.

Published in final edited form as:

Nat Neurosci. 2020 September ; 23(9): 1079–1089. doi:10.1038/s41593-020-0686-7.

Tau induces PSD95-nNOS uncoupling and neurovascular dysfunction independent of neurodegeneration

Laibaik Park[1], **Karin Hochrainer**[1], **Yorito Hattori**[1], **Sung Ji Ahn**[1], **Antoine Anfray**[1], **Gang Wang**[1], **Ken Uekawa**[1], **James Seo**[1], **Victoria Palfini**[1], **Ismary Blanco**[1], **Diana Acosta**[1,2], **David Eliezer**[1,2], **Ping Zhou**[1], **Josef Anrather**[1], **Costantino Iadecola**[1]

[1]Feil Family Brain and Mind Research Institute, Weill Cornell Medicine, New York, NY USA

[2]Department of Biochemistry, Weill Cornell Medicine, New York, NY USA

Abstract

Cerebrovascular abnormalities have emerged as a preclinical manifestation of Alzheimer's disease and frontotemporal dementia, diseases characterized by accumulation of hyperphosphorylated forms of the microtubule associated protein tau. However, it is unclear if tau contributes to these neurovascular alterations independent of neurodegeneration. We report that mice expressing mutated tau exhibit a selective suppression of neural activity-induced cerebral blood flow increases that precedes tau pathology and cognitive impairment. The dysfunction is attributable to reduced vasodilatation of intracerebral arterioles and is reversible by turning down tau production. Mechanistically, the failure of neurovascular coupling involves tau-induced dissociation of neuronal nitric oxide synthase from post synaptic-density-95 and reduced production of the potent vasodilator nitric oxide during glutamatergic synaptic activity. The data identify glutamatergic signaling dysfunction and nitric oxide deficiency as yet-undescribed early manifestations of tau pathobiology independent of neurodegeneration, and provide a mechanism for the neurovascular alterations observed in the preclinical stages of tauopathies.

Keywords

Alzheimer's disease; frontotemporal dementia; 2-photon microscopy; neurovascular unit; neurodegeneration; post-synaptic density

Alzheimer's disease (AD) is the major cause of age-related cognitive impairment for which there are no disease-modifying treatments at the present [1]. The failure of clinical trials

Correspondence Costantino Iadecola MD or Laibaik Park, PhD, 407 East 61st Street, RR-303, New York, NY 10065, T 646-962-8279, F 646-962-0535, coi2001@med.cornell.edu; lap2003@med.cornell.edu.

Author contributions

L.P., K.H. and Y.H. conducted the experiments and performed the data analysis; S.J.A. and A.A. conducted the two-photon microscopy and laser-speckle experiments; G.W. performed the NO production and Ca^{2+} imaging experiments; J.S. and K.U. contributed to the histology experiments; I.B. and V.P. contributed to the immunoprecipitation and Western blotting experiments; D.E. and D.A. provided WT recombinant tau; L.P., K.H., P.Z., J.A. and C.I. supervised the research; L.P., K.H. and C.I. provided funding; L.P. and C.I. wrote the manuscript.

Competing financial interest

CI serves on the advisory board of Broadview Ventures. The other authors have no conflicts to declare.

targeting the amyloid-β peptide (Aβ), a key pathogenic factor in AD, has emphasized the urgent need to pursue alternative features of AD pathology [2, 3]. Cerebrovascular dysfunction has recently emerged as an early manifestation of AD with a major impact on the evolution and clinical expression of the dementia [4-7]. But, most studies have focused on Aβ and little is known on the cerebrovascular effects of "pathological" species of tau (p-tau) [8], the other major culprit in AD [9]. Cerebrovascular alterations have also been described in neurodegenerative diseases, such as frontotemporal dementia (FTD) [10-12], characterized by p-tau accumulation without Aβ, raising the possibility that neurovascular dysfunction is an early pathogenic contributor to the disease process.

Since the brain lacks energy reserves, a vital role of the cerebrovascular network is to supply oxygen- and glucose-rich blood to active brain regions commensurate with their energy expenditures. This phenomenon, termed functional hyperemia or neurovascular coupling, matches the local delivery of cerebral blood flow (CBF) with the dynamic energy needs of the brain [8]. Disruption of neurovascular coupling may deprive brain cells of the needed energy substrates and, in the long run, lead to neuronal dysfunction and cognitive impairment [13, 14]. Glutamatergic synaptic activity initiates functional hyperemia by triggering nitric oxide (NO) production from neuronal NO synthase (nNOS), an enzyme linked to the NMDA receptor (NMDAR) complex through the scaffolding protein PSD95 [15-17]. In turn, NO, a potent vasodilator, acts on local microvessels to evoke the increase in flow [18-20]. Cerebrovascular alterations and synaptic dysfunction have been described in mouse models of human tauopathies, but most studies examined advanced stages of tau pathology [21-23]. Therefore, these alterations could be secondary to neurodegeneration rather than a driver of pathology. Furthermore, it is not known if p-tau, which is present at the PSD and may bind PSD components [23, 24], interferes with nNOS signaling to disrupt neurovascular coupling and, if so, whether such disruption precedes neuronal loss and cognitive dysfunction.

Here we examined the impact of p-tau on neurovascular function in mouse tauopathy models. We found that p-tau induces a profound and selective suppression of functional hyperemia that precedes neuronal loss and behavioral dysfunction. The effect was mediated by dampening neuronal NO production during NMDAR activation, resulting in impaired relaxation of the neocortical arterioles initiating the CBF increase. Co-immunoprecipitation studies indicated that p-tau disrupts the association between PSD95 and nNOS, and uncouples NMDAR activity from neuronal NO production. The findings unveil a previously-unappreciated harmful effect of p-tau on NMDAR signaling and neurovascular function in the presymptomatic stage of tau pathology, and raise the possibility that suppression of functional hyperemia and loss of other beneficial effects of NO may contribute to the cerebrovascular and brain dysfunction in tauopathies, such as AD and FTD.

Results

Tau disrupts neurovascular coupling prior to tangles and neurodegeneration

We used PS19 mice expressing mutated human tau (P301S) [25] to investigate the impact of p-tau on cerebrovascular structure and function. In some studies, we also used rTg4510 mice expressing the P301L tau mutation [26] to verify the results in another tauopathy model and,

since tau expression in rTg4510 mice is regulatable, to determine if the neurovascular phenotype is rescuable by suppressing tau expression. All mice were studied at 2-3 months of age to assess whether neurovascular dysfunction precedes the development of full-blown tau pathology, neurodegeneration and cognitive impairment [26-28]. Age-matched littermates served as wild type (WT) controls. At this age, PS19 mice showed a small reduction in resting cerebrocortical and hippocampal CBF, assessed quantitatively by ASL-MRI, whereas rTg4510 mice and their littermates, including WT mice or mice expressing only transactivator (TA) or human tau, exhibited no change (Fig. 1A; Extended data Fig. 1A-D). Neocortical thickness and hippocampal volume were not reduced both in PS19 and rTg4510 mice (Fig. 1B; Extended data Fig. 1A-D). Furthermore, although tau was phosphorylated at the AT8 site and displaced to somatodendritic compartments, no neurofibrillary tangles (thioflavin-S), neuronal loss (NeuN), or microvascular damage was observed (Fig. 1C; Extended data Figs. 2A-I, 3A, 4A-C). Microglia/macrophages (Iba1) were not increased, but enhanced astrogliosis (GFAP) was found in rTg4510 mice (Extended data Fig. 3B,C). Consistent with the lack of tau pathology and neurodegeneration and with previous reports [25, 26], no dysfunction was observed at the Barnes maze, novel object recognition or the Y-maze test (Fig. 1D-F), and no changes in locomotor activity were observed in both models (Extended data Fig. 5A).

We then examined neurovascular function in anesthetized mice equipped with a cranial window, in which CBF was monitored by laser-Doppler flowmetry (CBF-LDF) with controlled blood pressure and blood gases [20]. We found that the increases in CBF-LDF induced in the whisker barrel cortex by mechanical stimulation of the facial whiskers were markedly attenuated in PS19 mice (Fig. 1G). The attenuation observed under urethane-chloralose anesthesia (Fig. 1G) was also observed with isoflurane anesthesia (Extended data Fig. 5B). Surprisingly, the increase in CBF-LDF produced by bathing the cranial window with acetylcholine, bradykinin or the Ca^{2+} ionophore A23187, responses mediated by the release of vasoactive agents from cerebral endothelial cells [29], were not attenuated (Fig. 1H; Extended data Fig. 5C). Similarly, CBF-LDF increases evoked by agonists acting on vascular smooth muscles [adenosine or the NO donor S-Nitroso-N-acetyl-DL-penicillamine (SNAP)], or by hypercapnia, a powerful vasoactive stimulus in the cerebral circulation [30-32], were not affected (Extended data Fig. 5C), attesting to the integrity of the vasomotor apparatus. Identical results were obtained in rTg4510 mice (Fig. 1G,H; Extended data Fig. 5C).

Since tau is quickly internalized by neurons [33], we investigated if exogenous tau would reproduce the neurovascular effects observed in tau mice. We found that recombinant full-length WT (0.1-5μM) or mutant tau (P301L; 0.1-5μM) applied directly to the whisker barrel cortex of WT mice elicited neurovascular coupling dysfunction, but did not alter resting CBF-LDF or responses to acetylcholine and adenosine, mimicking the cerebrovascular phenotype of tau mice (Fig. 1I; Extended data Fig. 5D). Although the minimal effective concentration of tau applied to the neocortex (100-200nM) is higher than that estimated by microdialysis in the extracellular space of tauopathy models (3-4nM) [34], the concentration reaching the brain substance is likely to be significantly lower due to the diffusion gradient, oligomerization and pial membrane diffusion barriers [35, 36]. These observations establish that tau overexpression disrupts neurovascular coupling selectively, prior to the appearance

of neurofibrillary tangles, neurodegeneration, neurovascular damage or cognitive impairment.

The suppression of neurovascular coupling in tau mice results from impaired vasodilatation of intracerebral arterioles

Next, we investigated the microvascular bases of the suppression in functional hyperemia in tau mice. Functional hyperemia involves activity-induced dilatation of intracerebral microvessels followed by relaxation of upstream pial arterioles feeding the activated area [8]. The former is initiated by neurally-derived mediators including NO, and the latter by retrograde propagation of vasodilation via intramural vascular signaling [8, 19, 37, 38]. To define the microvascular changes responsible for the suppression of the hyperemic response we first used laser-speckle imaging (LSI) to pinpoint the neocortical site of maximal hyperemia and to identify the feeding pial arterioles (Fig. 2A). Then, we used two-photon microscopy (2PM) in the same mice to reconstruct the microvascular network supplying the activated area and assess the changes in vascular diameter induced by whisker stimulation in WT and tau mice (Fig. 2A). In WT mice whisker stimulation increased CBF-LSI in the activated whisker barrel cortex, which remained stable throughout the stimulation period (45 sec) (Fig. 2B top, shaded area). 2PM analysis revealed sustained increases in vascular diameter which were faster and larger in 1st, 2nd and 3rd order branches than in upstream parent pial arterioles feeding the activated area (Fig. 2B, top tracings; Fig. 2C, top). In PS19 mice, average CBF-LSI increases were blunted and were not sustained throughout the stimulation period (Fig. 2B bottom, shaded area; Fig. 2D). 2PM analysis did not reveal differences in the baseline diameter of the arteriolar network (Fig. 2C bottom), but the vasodilatation induced by whisker stimulation was suppressed in 1st, 2nd and 3rd order branches, with no significant reductions in upstream pial arterioles (Fig. 2B bottom; Fig. 2C top). However, while the time for the CBF response to reach 50% of maximum in 1st, 2nd and 3rd order branches did not differ between PS19 and WT mice, the vasodilatation of upstream pial arterioles developed more slowly in PS19 mice, and responses were generally less sustained (Fig. 2E-G). Therefore, the suppression of neurovascular coupling in tau mice results from reduced and less sustained vasodilatation of intracerebral arterioles and a delay in the vasomotor response of upstream pial arterioles.

The suppression in functional hyperemia is not due to attenuation of the neural activity driving the vascular response

Since neural activity initiates neurovascular coupling [8] and p-tau may suppress synaptic activity [23], we examined whether the attenuation in functional hyperemia in tau mice could be a consequence of reduced neuronal activation. However, the frequency distribution of the electrocorticogram and the amplitude of the field potentials evoked by stimulation of the whisker pad did not differ between PS19 and WT mice (Fig. 3A,B). Furthermore, using Fura2 as an indicator in dissociated neocortical neurons of 2-3-months-old PS19 mice, we found that the increase in intracellular Ca^{2+} induced by NMDAR activation, a major driver of the hyperemic response [8, 18, 20, 39], was not attenuated (Fig. 3C). Therefore, reduced neural activity cannot be responsible for the attenuation in functional hyperemia in 2-3 months-old tau mice.

Suppressing tau production rescues neurovascular coupling and prevents cortical atrophy and cognitive deficits in older rTg4510 mice

rTg4510 mice were engineered with a tetracycline-controlled transcriptional activator driven by the CaMKII promoter and a P301L tau transgene driven by a tetracycline operon-responsive element, such that administration of doxycycline turns down tau production [26]. We used this model to determine if suppressing tau production reverses the neurovascular coupling dysfunction and the other alterations observed in older rTg4510 mice. Starting at 3-4 months of age, tau production was turned down with doxycycline in the chow and CBF responses were tested 4 months later. Age-matched rTg4510 and WT littermates fed a regular diet, as well as WT mice treated with doxycycline, served as controls. rTg4510 mice (age 7-8 months) receiving control diet (tau-on) had reduced resting CBF in neocortex and hippocampus, impaired neurovascular coupling, reduced cortical thickness, neuronal loss, cognitive impairment and thioflavin-S-positive neurofibrillary tangles (Fig. 4A-F; Extended data Figs. 6A,B, 7A-C). CBF responses to adenosine and SNAP were not reduced (Extended data Fig. 7D). Therefore, as anticipated, aging tau mice exhibited full blown tau pathology, with neurodegeneration, neurovascular dysfunction and cognitive deficits. Doxycycline treatment (tau-off) reduced tau P301L mRNA (Extended data Fig. 6C) and rescued resting CBF and neurovascular dysfunction, as well as the other abnormalities observed in rTg4510 mice treated with control diet (Fig. 4A-F; Extended data Figs. 6B, 7A-C). Aquaporin 4 immunoreactivity, which labels astrocytic end-feet, was not disrupted in rTg4510 mice with or without doxycycline (Extended data Fig. 8A), indicating preservation of gliovascular associations. Furthermore, the astrogliosis observed in rTg4510 mice was not reduced with tau suppression despite the neurovascular and cognitive rescue, suggesting that it had no role in these alterations (Extended data Fig. 8B). As previously reported [26], doxycycline treatment did not prevent the development of neurofibrillary tangles (Extended data Fig. 6B). These observations link the neurovascular dysfunction to p-tau expression and support the involvement of more soluble tau species, rather than neurofibrillary tangles, in the deleterious neurovascular effects of p-tau [23].

Neurovascular dysfunction in tau mice is caused by uncoupling glutamatergic synaptic activity from neuronal NO production

Glutamatergic synaptic activity is a major driver of the increase in CBF produced by whisker stimulation [8, 20, 39]. Therefore, we asked whether the attenuation in functional hyperemia in tau mice is due to a deficit in the increase in CBF induced by glutamate receptor activation. In WT mice the increase in CBF-LDF induced by whisker stimulation, but not resting CBF-LDF and the increase induced by acetylcholine or adenosine, was attenuated by neocortical application of the NMDAR antagonist MK801 (Fig. 5A; Extended data Fig. 9A). However, in PS19 mice MK801 failed to attenuate the increase in CBF-LDF further (Fig. 5A). This finding suggests that the NMDA-dependent component of the CBF response is already totally suppressed in tau mice. Consistent with this hypothesis, the increase in CBF-LDF induced by bathing the whisker barrel cortex with NMDA (40 μM), but not AMPA (10 μM), was blunted in PS19 mice and could not be attenuated further by MK801 (Fig. 5B,C). Similar results were obtained in rTg4510 mice (Fig. 5A-C). P-tau has been reported to reduce glutamate receptor expression, trafficking and function [23]. However, the reduced CBF-LDF response was not related to alterations in NMDAR subunit expression (Extended

data Figs. 9B and 10A-C) or to failure of the receptor to flux Ca^{2+} in response to NMDA (Fig. 3C).

Since NO derived from nNOS plays a key role in the increases in CBF induced by NMDAR activation and whisker stimulation [18-20, 40], we examined whether the NO-dependent component of these responses was suppressed in tau mice. Neocortical application of the broad-spectrum NOS inhibitor L-nitroarginine (L-NNA; 100μM), attenuated resting CBF-LDF and the increase produced by whisker stimulation or NMDA in WT, but not in PS19 mice (Fig. 6A-C). However, attesting its effectiveness, L-NNA attenuated the increase in CBF-LDF produced by neocortical application of acetylcholine, a response mediated by eNOS, both in WT and PS19 mice (Fig. 6D). CBF responses to adenosine were not affected (Fig. 6E). These data suggest that the component of functional hyperemia mediated by neuronal NO is attenuated in tau mice.

To provide further evidence in support of this possibility we assessed NO production using the indicator DAF-FM in dissociated cortical neurons exposed to NMDA (40μM) [18, 41]. We found that NMDA increases NO production in neocortical neurons isolated from WT mice but not from 2-3 months-old PS19 or rTg4510 mice (Fig. 7A). Attesting to NO being the source of the DAF-FM signal, the increase in NO induced by NMDA was blocked by the NOS inhibitor L-NNA (Extended data Fig. 9C).The attenuation in NMDA-induced NO production was also observed in cortical brain slices of PS19 mice in which NO was measured amperometrically (Fig. 7B) [20]. As in tau mice, pre-treatment with full-length recombinant tau (P301L; 400nM) suppressed NO production in WT neurons exposed to NMDA (Fig. 7C). The suppression of NMDA-induced NO production was not a consequence of reduced expression of GluN2B, PSD95 and nNOS protein, or their localization to synaptosomes or postsynaptic density (PSD), because their levels did not differ between WT, PS19, and rTg4510 mice (Extended data Fig. 10A-C). Nor was the effect due to suppression of the increase in intracellular Ca^{2+} induced by NMDA, which drives neuronal NO production (Fig. 3C). In addition, levels and localization of synaptophysin and MEK1/2 (Extended data Fig. 10B) as well as the protein level and activity of Ca^{2+}-calmodulin kinase IIα, an enzyme involved in NMDA receptor signaling, were not altered in PS19 mice (Extended data Fig. 10D). These observations indicate that the attenuation in functional hyperemia in tau mice is mediated by a dissociation between NMDAR activity and neuronal NO production, resulting in suppression of the NO-dependent component of the vasodilatation.

Tau overexpression leads to dissociation of nNOS from the NMDAR-PSD95 complex

The GluN2B subunit of the NMDAR is linked to nNOS through the adaptor protein PSD95 [15, 17] and disruption of their association uncouples NMDAR activity from NO production [18, 20, 42]. Therefore, we asked whether tau overexpression suppresses NO production by altering the interaction of nNOS with the NMDAR complex. First, we sought to determine if tau is present at the PSD. We found an increase in total tau, as well as phosphorylated tau (AT8, PHF13) in PSD preparations from 2-3 months-old PS19 compared to WT mice (Fig. 7D). Next, we investigated by co-immunoprecipitation in PSD preparations if the association of GluN2B with PSD95 and/or PSD95 with nNOS is disrupted in PS19 mice. We found that

both WT and PS19 mice have comparable levels of GluN2B bound to immunoprecipitated PSD95, demonstrating that the association of GluN2B to PSD95 was not altered by p-tau (Fig. 7E). However, immunoprecipitation of nNOS revealed a marked reduction of its association with PSD95 in PS19 mice (Fig. 7F), suggesting that the decrease in the NMDAR-induced production of neuronal NO in tau mice correlates with a disruption of the link between the NMDAR-PSD95 complex and nNOS.

Tau binds to PSD95 and disrupts the association between PSD95 and nNOS

To address whether tau is capable of disrupting PSD95-nNOS association by direct binding we exogenously expressed these proteins in HEK293T cells and performed co-immunoprecipitation studies. Overexpression of both WT and P301L tau resulted in hyperphosphorylated tau, determined by phosphatase-sensitive detection with the p-tau antibody AT8 (Fig. 8A, Extended data Fig. 10E). nNOS efficiently bound to immunoprecipitated PSD95, which was significantly reduced when tau was present (Fig. 8B, Extended data Fig. 10F). Tau co-precipitated with PSD95-nNOS (Fig. 8B, Extended data Fig. 10F), suggesting that it directly binds either to nNOS or PSD95 to weaken their association. To test this hypothesis, we first examined if nNOS co-precipitates with tau after co-expression in HEK293T cells, but we did not observe an interaction (Fig. 8C). However, when we co-expressed PSD95 with tau we found that tau binds to precipitated PSD95 (Fig. 8D, Extended data Fig. 10G), suggesting that the disruption of PSD95-nNOS association is due to tau binding to PSD95.

Discussion

We have demonstrated that tau-expressing mice have a selective suppression of the hyperemia produced by neural activity, while the CBF increases initiated by agonists acting on the endothelium or smooth muscle are not impaired. The neurovascular dysfunction is independent of neurodegenerative changes or cognitive deficits, which were not observed at this early age. Pharmacological studies suggested that the neurovascular dysfunction is a consequence of reduced NO production evoked by the glutamatergic synaptic activity driving the hyperemic response, a hypothesis confirmed by *ex vivo* studies in dissociated neurons demonstrating reduced NO production during NMDAR activation. The effect was not due to reduced Ca^{2+} influx during NMDAR activation, or to downregulation of the expression of receptor subunits, PSD95 or nNOS, as reported in more advanced stages of tau pathology [23, 43, 44]. Rather, we observed a disruption of the association of nNOS with PSD95 well known to result in suppression of NMDAR-induced NO production [18, 20, 42]. Consistent with previous studies, uncoupling NMDAR from nNOS did not alter resting NO levels, but it attenuated the NO increase induced by NMDAR activation [18, 20]. The signaling dysfunction does not result from a global disruption of the PSD since the association between PSD95 and GluN2B was not reduced, but can be attributed to the binding of mutated tau to PSD95, in turn, leading to dissociation of nNOS from GluN2B-PSD95 complex (Extended data Fig. 10H). To our knowledge, the uncoupling of NO production from glutamatergic synaptic activity described here may be the earliest alteration in synaptic function induced by p-tau thus far described *in vivo*.

Recent evidence suggests that insertional effects of multiple copies of the transgenes in rTg4510 mice result in genomic deletion of 244Kb of the fibroblast growth factor-14 gene and of several other genes [45, 46]. It has also been reported that in a new mouse line in which a single copy of the same P301L transgene was targeted to an intergenic site previously demonstrated to promote transgene expression without dysregulating endogenous gene expression, brain atrophy occurred at a pace slower than in rTg4510 mice, despite much higher levels of tau [45]. Therefore, the insertional effects in rTg4510 mice are likely to accelerate the brain volume loss independently of tau. For the following reasons, however, we believe that these alterations do not compromise the validity of our findings in rTg4510 mice. First, the selective suppression of functional hyperemia observed in rTg4510 mice was replicated in two additional models: PS19 mice and WT mice with neocortical application of tau. Second, the accelerating effect on cortical atrophy was observed in 8-7-month-old rTg4510 mice, whereas neurovascular dysfunction was already present at 2-3 months of age when, despite the genomic disruption, no structural or behavioral alterations were observed in rTg4510 mice. Third, turning off tau production with doxycycline reversed the neurovascular dysfunction in 8-7-month-old rTg4510 mice despite the genomic disruption. Collectively, these findings link the neurovascular dysfunction to tau and not to the consequence of the genomic deletions in rTg4510 mice.

The microvascular basis of the failure of neurovascular coupling in tau mice is related to a reduced response to neural activity of higher order pial arteriolar branches supplying the activated whisker barrel cortex. Considering that intracerebral arterioles are the major target of neuronal NO released during activation [19], the reduced responsivity of these vessels is consistent with the deficit in neuronal NO induced by p-tau. Interestingly, the vasodilatation of pial arterioles was not attenuated, but exhibited a slower time course, probably reflecting the attenuated stimulus driving the conducted vasodilation from the intracerebral arterioles [8]. While these observations identify intracerebral arterioles as the microvascular site responsible for the reduced hyperemic response, they also reveal a unique vascular segment selectivity of the neurovascular dysfunction induced by p-tau.

The effects of p-tau on neurovascular coupling are independent of neurofibrillary tangles. Thus in 2-3 months-old rTg4510 and PS19 mice neurovascular dysfunction was present in the absence of tangles. Furthermore, when tau production was reduced in rTg4510 mice, neurovascular function was rescued despite the persistence of neurofibrillary tangles, which persisted despite the suppression in tau expression [26]. These observations indicate that the effects of p-tau on functional hyperemia are related to less insoluble tau species. In support of this conclusion, we found association of tau with PSD95 in 2-3 months-old tau mice without tangles or other aspects of tau pathology. Furthermore, expression of WT or mutant tau in HEK293T cells prevented the association of PSD95 with nNOS. These observations reinforce the notion that less insoluble forms of tau are responsible for the signaling abnormality underlying the neurovascular dysfunction [26]. Of note, both WT and mutant tau were phosphorylated at the AT8 site, but it remains unclear if phosphorylation or aggregation is needed for tau to induce PSD95-nNOS uncoupling. Furthermore, it would be of interest to determine if, after suppressing tau production, the rescue of neurovascular coupling precedes the cognitive improvement, suggesting that improved vascular function contributes the improved cognition.

Tau mice have long been described to exhibit altered glutamate receptor subunit expression, trafficking, and currents [23, 43, 44]. However, most investigations were performed in advanced disease, and it could not be determined if these alterations were the cause or the result of neurodegeneration. Hoover et al. described downregulation of NMDAR expression and trafficking preceding neurodegeneration in 4 months-old rTg4510 mice [27]. The present study establishes that p-tau alters NMDAR signaling even earlier, and without suppressing glutamate receptor subunits, PSD95, nNOS, or NMDA-induced intracellular Ca^{2+} rise, but by uncoupling NMDAR activity from NO production. The role of the resulting deficit in NO production in the harmful effects of p-tau on brain function and cognition remains to be established. The alterations in neurovascular coupling could impair energy homeostasis and lower the threshold to injury caused by tau itself or other factors [8, 14]. In addition, the loss of NO's role in neurotransmission, long-term potentiation, synaptic plasticity and neurogenesis may also contribute to impaired brain function [47]. The NO deficit could also lead to presynaptic dysfunction, due to the role of NO as a retrograde messenger [48]. Finally, other PSD95 binding partners, including transmembrane, signaling, and cytoskeletal proteins, could also be displaced leading to potentially deleterious consequences [49]. These alterations may act synergistically with the other harmful effects of p-tau and, in the long run, cause brain dysfunction and promote neurodegeneration. Irrespective of the impact of the neurovascular effects of tau, the observation that cerebrovascular dysfunction is observed in the preclinical stage of tauopathies such as FTD [10, 12], supports the notion that the neurovascular effects of tau described in the present study are relevant to the human disease and could play a pathogenic role in the early stages of the disease process.

In conclusion, we have demonstrated that mice overexpressing mutated tau exhibit a selective disruption of neurovascular coupling, that can be ascribed to a failure of intracerebral arterioles to relax in response to glutamatergic synaptic activity. The neurovascular dysfunction is observed prior to formation of neurofibrillary tangles and neurodegeneration, and can be reversed by downregulating tau expression, despite persistence of tangles. The uncoupling of neural activity from CBF is a consequence of the failure of NMDAR activation to evoke NO production, an effect resulting from the association of p-tau with PSD95 which disrupts the link between nNOS and the GluN2B-PSD95 complex. The data identifies alterations in NMDAR signaling as an early consequence of tau pathobiology, which may play a role in brain dysfunction and ensuing neurodegeneration. Furthermore, the data provide the mechanistic bases for the neurovascular alterations reported in the pre-symptomatic stage of tauopathies and raise the novel possibility that restoring NMDAR-dependent NO production may help counteract some of the harmful consequences of p-tau accumulation.

Materials and Methods

Mice

All procedures were approved by the Institutional Animal Care and Use Committee of Weill Cornell Medicine and performed according to the ARRIVE guidelines [50]. Experiments were performed in two tau transgenic mouse lines: rTg4510 (P301L) [26] and PS19 (P301S) [25] (Jackson Lab stock# 008169) mice. The bi-transgenic rTg4510 mice were generated with

conditional tau P301L expression driven by the CaMKIIα promoter by crossing responder (tau; The Jackson Lab stock# 015815) and transactivator (TA; The Jackson Lab stock# 007004) transgenic lines. To suppress tau transgene expression, rTg4510 mice were fed ad libitum with doxycycline (200 mg/kg; Product# S3888; Bio-Serv, Flemington, NJ) or control diet (Product#S4207; Bio-Serv, Flemington, NJ) starting at 3-4 months of age for 4 months. All tau transgenic mice and wild type littermates were males.

Magnetic resonance imaging

Imaging was performed on a 7.0 Tesla 70/30 Bruker Biospec small animal MRI system with 450 mT/m gradient amplitude and a 4,500T/m/s slew rate, as previously reported [41]. Briefly, the animals were anesthetized with isoflurane (1-2%) and placed in the MRI. A volume coil was used for transmission and a surface coil for reception. The magnet coordinate of each animal varied a bit between mice, but the anatomical slice package was always aligned in the same way on each mouse, with the final slice in the forebrain right before the olfactory bulb. This allowed to consistently landmark the anatomical images and then center the ASL slice package a set distance from the anatomical slice package. Anatomical localizer images were acquired to find the transversal slice corresponding to the somatosensory cortex [51]. This position was used for subsequent ASL imaging, which was based on a flow-sensitive alternating inversion recovery rapid acquisition with relaxation enhancement (FAIR-RARE) pulse sequence labeling the inflowing blood by global inversion of the equilibrium magnetization. Three averages of one axial slice were acquired with a field of view of 15 × 15 mm, spatial resolution of 0.234 × 0.234 × 2 mm^3, echo time TE of 5.368 ms, effective TE of 26.84 ms, repeat time TR of 10 s, and a rapid imaging with refocused echoes (RARE) factor of 36. For computation of CBF, the Bruker ASL perfusion processing macro was used [52]. Turbo-RARE anatomical images were acquired with the same field-of-view and orientation as the ASL images (resolution = 0.078 × 0.078 × 1 mm^3, TE = 48 ms, TR = 2000 ms, and a RARE factor of 10). The total scan time (ASL+anatomical images) was 39 min. The ASL- and T2-MRI images were evaluated for resting CBF and cortical and hippocampal anatomy, respectively, at the bregma level of −1.70 mm [51] using ImageJ 1.52r (NIH). The average CBF value is reported as ml/100 g of tissue/minute (ml/100g/min). To measure cortical thickness, 2-3 measurements were taken bilaterally in a coronal section at different levels from the midline and averaged to produce mean thickness in mm [41]. To measure hippocampal volume, the regions of interest (ROI) representing the right and left hippocampi were drawn on T2-weighted coronal sections and measured. The hippocampal volume (mm^3) was then calculated using the following formula: the hippocampal volume = sum of ROI x .0.5 mm (a thickness of a T2-MRI section).

General surgical procedures for CBF-LDF measurement

As described in detail elsewhere [20, 53, 54], mice were anesthetized with isoflurane (induction, 5%; surgery, 2%) and maintained with urethane (750 mg/kg; i.p.) and α-chloralose (50 mg/kg; i.p.). A femoral artery was cannulated for recording of arterial pressure and blood gas analysis. A feedback-controlled heating pad was used to maintain body temperature at 37°C. The trachea was intubated and mice were artificially ventilated with a mixture of N_2 and O_2. Throughout the experiment the level of anesthesia was monitored by testing motor responses to tail pinch. The somatosensory cortex was exposed through a small craniotomy

(2x2 mm). The dura was removed, and the exposed cortex was continuously bathed with a modified Ringer's solution (36-37°C; pH: 7.3-7.4) (see ref Iadecola (1992) [55] for composition). CBF was continuously monitored at the site of superfusion with a laser-Doppler probe (Vasamedic) positioned stereotaxically on the neocortical surface and connected to a computerized data acquisition system. CBF values were expressed as percent increase relative to the resting level. Resting CBF is reported as arbitrary laser-Doppler perfusion units. As a control, zero values for CBF were verified after the heart was stopped by an overdose of isoflurane at the end of the experiment.

Experimental protocol for CBF-LDF measurement in open cranial windows

CBF recordings were started after arterial pressure and blood gases were in a steady state. Arterial blood pressure (80-90 mmHg), blood gases (pO_2, 120-140 mmHg; pCO_2, 30–40 mmHg; pH, 7.3-7.4) were monitored and controlled. Blood gases were measured twice using a blood gas analyzer [Siemens (Chiron Diagnostics) M248, Deerfield, IL] to assure their stability. All pharmacological agents were dissolved in a modified Ringer's solution. CBF-LDF responses to mechanical stimulation of the whiskers at 5 Hz for 60 sec were recorded. To test endothelium-dependent responses acetylcholine (10 μM, Sigma), the Ca^{2+} ionophore A23187 (3 μM; Sigma) or bradykinin (50 μM; Sigma) was topically superfused for 3-5 min and the evoked CBF-LDF increases recorded. To test smooth muscle reactivity, CBF-LDF response to adenosine (400 μM, Sigma) or the NO donor SNAP (50 μM, Sigma) were examined [20, 54, 56]. The increase in CBF-LDF produced by hypercapnia was tested by introducing 5% CO_2 in the ventilator to increase arterial pCO_2 up to 50-60 mmHg for 3-5 min. In some experiments the CBF-LDF response to NMDA (40 μM; Sigma) or AMPA (10 μM; Sigma) superfusion was tested [20]. To test effect of topical application of recombinant tau (rTau) on functional hyperemia, the cranial window was superfused with a Ringer's solution containing rTau [Tau-411 (2N4R) P301L mutant, rPeptide; 0.1-5 μM]. rTau was freshly reconstituted in distilled water and then diluted in normal Ringer's solution. The CBF-LDF response to whisker stimulation, ACh, and adenosine was tested 30-40 minutes after rTau superfusion. In some experiments, the CBF-LDF response to whisker stimulation, ACh, NMDA, AMPA, or adenosine was tested before and 30 minutes after superfusion of the cranial window with the NMDA receptor antagonist MK-801 (10 μM; Sigma) or the nonselective NOS inhibitor L-NNA (1 mM; Sigma). In experiments with MK-801 pretreatment, the effect of the Na^+ channel blocker TTX (3 μM; Sigma) was also tested.

Protocol for CBF-LSI and 2-Photon imaging

Procedures for cranial window and thinned skull preparations were described previously [41, 57, 58]. In brief, mice were anesthetized with isoflurane and secured on a stereotaxic frame equipped with a heating pad. After removing the scalp and periosteum from the surface of the skull, a custom-made titanium head post was glued onto right hemisphere over the somatosensory cortex. The skull was thinned using a dental drill and the surface was then covered with a thin layer of cyanoacrylate adhesive. Mice were then anesthetized with urethane and α-chloralose (see above). The trachea was intubated for mechanical ventilation. In selected mice, the femoral artery was cannulated to monitor arterial pressure and blood gases to assure that these variables were in the range described above for CBF-LDF.

CBF-LSI imaging: CBF-LSI was performed with a commercial system (Omegazone; Omegawave) [41, 59]. Thinned skull was illuminated with a semiconductor laser set at 780 nm and the scattered light was detected with a CCD camera positioned over the skull. Color-coded CBF images were obtained in highest resolution (639 × 480 pixels) with the sampling frequency at 60 Hz. Each recording lasted for 135 seconds of which 3 periods included baseline, whisker stimulation, and recovery (45 sec each) to monitor a full course of CBF change (see Fig. 2A for representative images). Images were obtained for each period separately for off-line quantification. Two regions of interests (ROI) were selected, one placed within the whisker barrel cortex and another one outside the barrel cortex, to monitor CBF changes and select candidate vessels to image by 2-photon microscopy.

2-photon imaging: After selecting the candidate vessels under LSI imaging, mice were injected with fluorescein dextran-conjugated dye (2.5% w/v FITC 70 kDa) diluted in sterile saline via retro-orbital injection (50 μl) to visualize the vasculature [41, 57]. Imaging was performed on a commercial two-photon microscope (Fluoview FVMPE; Olympus) equipped with a solid-state laser (InSight DS+; Spectraphysics) set to a 800-nm wavelength. Image stacks were acquired through Fluoview software (FV31S-SW, version 2.3.1.163; Olympus). First, a map of vasculature was taken through a 5x objective (MPlan N 5x 0.1 NA; Olympus) and compared with LSI images to locate the same imaging field in the whisker barrel cortex and to identify vessels branching from pial arteries at the cortical surface that feed barrel area. Once the blood vessels to be imaged were identified, we switched to a 25x objective (XLPlan N 25x 1.05 NA; Olympus), which was mounted on a piezo motor stage (P-725 PIFOC; PI) for higher resolution, rapidly-repeated z-stack imaging. To measure time-dependent changes in vessel diameter, we took rapid z-stacks (< 2 s per stack) centered on a vessel of interest, which varied in depth between 50 and 100 μm, with a z-step size between 5 and 20 μm and ~1 μm/pixel lateral resolution. An individual recording lasted for 2 minutes and 30 seconds and included baseline (60 s), whisker stimulation (45 s), and recovery (45 s). In each animal, stacks were taken at 3 to 6 regions within the barrel cortex and contained vessels of different sizes and classes of arterial branches.

Data analysis for LSI and 2-Photon imaging: For the analysis of LSI signal changes, ImageJ (NIH) was used. First, to obtain the net increase in LSI signals evoked by whisker stimulation, the average LSI signals acquired during baseline (60 s) was subtracted from the average LSI signals obtained during stimulation (45 s). Then, circular ROIs were drawn on the responsive areas in the images acquired during baseline and stimulation, and the CBF-LSI increase (%) produced by the whisker stimulation was calculated. For 2-photon data analysis, we first took each individual rapid z-stack and calculated a maximum intensity z-projection. Successive z-projections of the same vessel sets were then registered to each other using the ‘rigid body transformation’ under ImageJ (NIH) TurboReg plugin to remove spatial drift. In a few datasets, the spatial drift was too large for this registration and we, instead, analyzed subsets of the movie (each of which could be motion corrected) separately. After motion artifact correction, the z-projections were smoothed using a 3X3 pixel kernel and the contrast was manually adjusted with one setting for the entire movie, while avoiding saturation. To determine vessel diameter, line ROIs were manually drawn across the vessel of interest and fluorescent intensity profiles of the line ROI over time were exported for

further analysis using custom written MATLAB code. This yielded a time-dependent vessel profile, which was smoothed in both space and time with an averaging filter with a 1.5 pixel kernel size. The vessel diameter was measured at the time of each z-stack by interpolating the spatial profile by about 30X to smooth pixilation and calculating the full width at half maximum. Baseline diameter was calculated as the average diameter over 15 s before the onset of whisker stimulation and the percent diameter change was calculated from the baseline and the peak vessel diameter seen during whisker stimulus.

Electrocorticogram and field potentials

Mice were anesthetized and surgically prepared as described above. The electrocorticogram (ECG) was recorded by using bipolar recording electrodes positioned stereotaxically on the left somatosensory cortex (3 mm lateral and 1.5 mm caudal to bregma; depth of 0.6 mm) [20, 60]. The ECG was recorded for five epochs each lasting 5 min and separated by a 20-min interval. The timing of the recordings relative to the administration of anesthesia was identical for all animals. Signals were amplified, digitized, and stored (PowerLab; AD Instruments). Spectral analysis of the EEG was performed by using a software module embedded in PowerLab. Field potentials were recorded by using an electrode placed in the somatosensory cortex contralateral to the activated whiskers. The somatosensory cortex was activated by electrical stimulation of the whisker pad (2 V; 0.5 Hz; pulse duration, 1 ms). Analyses were performed on the average of 10 stimulation trials [61].

Ca^{2+} imaging and NO production

As described previously [41, 54, 62, 63], coronal cortical slices (350 μm in thickness) were cut from the brain of 2-3 months old WT and PS19 mice and incubated aCSF containing Pronase 0.02% (w/v), thermolysin (0.02%) at 36 °C (Sigma Aldrich). Neocortical neurons were then mechanically dissociated for Ca^{2+} imaging and assessment of NO production.

Ca^{2+} imaging: Dissociated neurons were incubated with the Ca^{2+} indicator Fura-2/AM (20 μmol/l, Life Fisher) [41, 54]. Fura-2/ AM-loaded cells were transferred to polyornithine-coated glass-bottom Petri dish (Warner Instruments, CT). Images were acquired on a Nikon 300 inverted microscope with an oil-immersion lens (Nikon CF UV-F X40; N.A., 1.3). Fura-2/AM was alternately excited through narrow bandpass filters (340 and 380 nm). An intensified CCD camera (Retiga ExI) recorded the fluorescence emitted by the indicator (510±4 nm). After background subtraction, fluorescence measurements were obtained from cell bodies of 3–5 neurons in randomly selected fields before and after perfusion of the cells with NMDA (40 μM) for 20 min. Fluorescence ratios (340/380 nm) were calculated for each pixel by using a standard formula [64]. At the end of the experiment, the viability of the preparation was verified by testing the Ca^{2+} response to the Ca^{2+} ionophore A23187 [54].

NO detection by DAF-FM: Dissociated neurons were incubated with DAF-FM (5 μM) in oxygenated l-aCSF for 30 min, and then rinsed in control buffer [41, 62, 63]. Time-resolved fluorescence (FITC filter) was measured at 30-s intervals with a Nikon diaphot 300 inverted microscope equipped with CCD digital camera (Princeton Instruments) and using IPLab software (Scanalytics). DAF-FM fluorescence intensity is expressed as Ft/Fo, where Fo is the baseline fluorescence before application of NMDA, and Ft is fluorescence in the same

cell after application of NMDA. Suppression of the NMDA-induced increase in NO by NOS inhibition with L-NNA (100μM) provided evidence that NO is the source of the signal (Extended data Figure 9C). In recombinant tau experiments, concurrent vehicle recordings were performed.

Amperometric NO detection: NO production was assessed by using an Apollo 4000 Analyzer equipped with a NO sensitive carbon fiber electrode (tip diameter, 0.1 μm; ISO-NOPNM; World Precision Instruments), as previously described [20]. The NO detection limit of the electrode is 0.5 nM with a response time <3s. After calibration of the electrode with the NO donor SNAP [20], NO production was assessed in neocortical slices of 2-3-month-old PS19 and WT mice. Brain slices were perfused with Mg^{2+}-free lactic acid artificial cerebrospinal fluid (aCSF; in mM: 121 NaCl, 5 KCl, 2 CaCl2, 0.01 glycine, 1 Na-pyruvate, 20 glucose, 26 NaHCO3, 1 NaH2PO4, 4.5 lactic acid, 95% O2 and 5% CO2, pH = 7.4) at room temperature. Perfusion of the aCSF was discontinued and the tip of the electrode was placed close to the surface of the slice. After stabilization of the basal NO signal, NMDA (100 μM in aCSF) was applied and the production of NO was monitored for at least 12 min. After washing off the NMDA, the NO production returned to baseline. The data were digitally acquired and stored for off-line analysis.

Immunohistochemistry

Mice were sacrificed by an overdose of sodium pentobarbital (120 mg/kg, i.p.) and perfused transcardially with PBS followed by 4% paraformaldehyde (PFA) in PBS. Brains were sectioned in a vibratome (section thickness: 40 μm). Free floating sections were permeabilized with 0.5% Triton X-100 and non-specific binding was blocked with 1% of normal donkey serum. Sections were randomly selected and incubated with the primary antibodies (see Supplementary Table 1). After washing, brain sections were incubated with a Cy5- or a FITC-conjugated secondary antibody (1:200; Jackson ImmunoResearch Laboratories), mounted on slides and imaged with a confocal microscope (Leica SP8). The specificity of the immunofluorescence was verified by omission of the primary and/or secondary antibody or blocking of the antigen. All quantifications were performed by investigators in blinded to the genotype of the mice on randomly selected fields within the somatosensory cortex.

Real-time PCR for NMDA receptors and tau

Quantitative determination of gene expression was performed on a Chromo 4 detector (Peltier thermal cycler; MJ Research) using a two-step cycling protocol. Primers are listed in Supplementary Table 2. Two microliters of diluted cDNA (1:10) were amplified by Platinum SYBR green qPCR supermix UDG (Invitrogen). The reactions were incubated at 50°C for 2 min and then 95°C for 10 min. A PCR cycling protocol consisting of 15 s at 95°C and 1 min at 60°C for 45 cycles was required for quantification. Quantities of all targets in test samples were normalized to the mouse housekeeping hypoxanthine-guanine phosphoribosyltransferase (HPRT) gene [52].

Western blotting and immunoprecipitation

Cytosolic-, membrane- and PSD-enriched protein isolation from brain lysates: Mouse forebrains were homogenized in 500μl ice-cold homogenization buffer [in mM: 15 Tris.HCl pH7.5, 250 sucrose, 1 $MgCl_2$, 2.5 EDTA, 1 EGTA, 1 dithiothreitol, protease inhibitors (Roche Applied Biosciences) and PhosSTOP (Sigma Aldrich)] per hemisphere through 30 strokes in a glass Dounce Homogenizer. Lysates were centrifuged at 10,000rpm for 10min at 4°C to obtain cytosolic supernatants. Pellets were resuspended in 250μl homogenization buffer, sonicated (20% amplitude for 10sec at 4°C; Branson Sonifier) and after addition of 2% Triton X-100 and 150mM KCl final concentration rotated for 60min at 4°C. Lysates were spun for 10min at 13,000rpm to separate the detergent-soluble membrane fraction from the detergent-insoluble PSD-enriched fraction. Presence of proteins in fractions was determined by Western Blotting with the primary antibodies (see Supplementary Table 1).

Co-immunoprecipitation studies from PSD-enriched brain lysates: The PSD fraction was solubilized by sonication for 10sec at 20% amplitude in 10 volumes 50mM Tris.HCl pH 7.5, 2% sodium dodecyl sulfate (SDS) and spun for 1hr at 13,300rpm. Chaps was added to supernatants in a final concentration of 0.1%, and SDS was precipitated by addition of 1/20 volume SDS-Out reagent (Thermo Fisher Scientific), incubation for 20min at 4°C and centrifugation for 10min at 10,000rpm. For renaturation of proteins, supernatants were diluted with 1/3 volume of 100mM Tris.HCl pH 7.5, 2.4% Tween-20, protease inhibitors, and PhosSTOP and were then incubated for 1.5hrs at 4°C. Thereafter, samples were added with 1/4 volume of 3.06% artificial chaperone cycloamylose [65] (Sigma Aldrich) and were incubated overnight at 4°C, spun at 13,000rpm for 15min and supernatants containing solubilized PSD proteins were collected. Twenty (20) μg of total protein was set aside as expression control. To assess PSD95-GluN2B interaction, 400μg lysate was diluted 1:1 with 1x phosphate buffered saline (PBS), combined with 4μg PSD95 antibody (clone G6G-1C9; Thermo Fisher Scientific) and incubated with agitation overnight. Subsequently, 60μl Dynabeads Protein G (Thermo Fisher Scientific) were added and samples were rotated for 2hrs at 4°C. nNOS association with PSD95 was determined by pull down with nNOS antibody (PA3-032A; Thermo Fisher Scientific) using the same protocol as above. Samples exposed to isotype control antibodies (BioLegend) were used as non-specific binding control. Beads were washed 3 times with 1x PBS and finally resuspended in 30μl SDS sample buffer (62.5mM Tris.HCl pH6.8, 2% SDS, 10% glycerol, 0.002% bromophenol blue, 50mM DTT). Proteins were resolved by 4-12% Tris-Glycine protein gels (Thermo Fisher Scientific), transferred to PVDF membranes (EMD Millipore) and detected by Western Blotting with antibodies against PSD95, nNOS and GluN2B.

Preparation of purified synaptosomes: Synaptosomes were isolated from forebrains as described [66]. All procedures were carried out at 4°C with pre-cooled reagents and equipment. All buffers were supplemented with protease and phosphatase inhibitors. Brains were homogenized in 1ml sucrose buffer (in mM: 320 mM sucrose, 1 $NaHCO_3$, 1 $MgCl_2$, 0.5 $CaCl_2$)/30mg tissue in a glass Dounce homogenizer with 12 strokes on ice. The homogenate was centrifuged at 2,500rpm for 10min to remove cell debris and nuclei. Pellet was re-homogenized in sucrose buffer and spun again. Supernatants were combined and

cleared from any residual debris by spinning at 1,200rpm for 10min. Cleared supernatants were subsequently centrifuged at 9,000rpm to obtain cytosolic supernatant and a pellet containing crude synaptosomes. Pellet was resuspended in 400µl sucrose buffer, pipetted onto 1.8ml 5% Ficoll-400 (Sigma Aldrich), and spun for 45min at 19,300rpm. The supernatant was removed and pellet was re-homogenized in 400µl 5% Ficoll-400. The homogenate was layered on 1.8ml 13% Ficoll-400 and again spun for 45min at 19,300rpm. Synaptosomes form a layer at the interface of 5% and 13% Ficoll-400. The layer was carefully removed and diluted to 1ml with 2% Ficoll-400.Then, synaptosomes were pelleted by centrifugation at 32,000rpm for 30min, after which they were taken up in 100µl 5% SDS, followed by sonication for 10sec at 20% amplitude.

CaMKII activity measurements: CaMKII activity was determined in cytosolic-, membrane- and PSD-enriched forebrain lysates using the highly selective peptide substrate Autocamtide-2 (peptide amino acid sequence: KKALRRQETVDAL). Fresh forebrain was homogenized in ice-cold 500µl lysis buffer (in mM: 50 Tris.HCl pH7.5, 150 NaCl, 0.25 DTT, 0.1 EDTA, 0.1 EGTA, 25% glycerol, protease and phosphatase inhibitors) per hemisphere by 15 strokes using a glass Dounce homogenizer. Lysates were centrifuged for 10min at 13,000rpm and the supernatant kept as cytosolic fraction. The pellet was resuspended in 250µl lysis buffer plus 2% Triton X100 and 150mM KCl and homogenized again. After 30min incubation on ice and spinning for 10min at 13,000rpm, the supernatant containing the membrane fraction was set aside. The PSD-enriched fraction was re-homogenized in 250µl lysis buffer, ensuring solubilization of all particles. Phosphorylation reactions were initiated by mixing 5µg lysate with 40µl reaction buffer containing 50mM HEPES.KOH pH7.4, 5mM $MgCl_2$, 0.05% BSA, 50µM substrate, 50µM ATP, 1mM $CaCl_2$, 2µM calmodulin and 5 Ci/mmole γ^{32}P-ATP (Perkin Elmer). Reactions were incubated at 30°C for 1min, after which they were terminated by spotting on P81 phosphocellulose cation exchange chromatography paper (Whatman). Filters were washed 4 times for 2min in 0.5% phosphoric acid, and the remaining radioactivity was quantified in a LS3801 scintillation counter (Beckman Coulter) by the Cherenkov method.

Plasmid constructs: PSD95 was amplified from C57BL6/J mouse cDNA with primers containing *Eco*RI (5'- gcacGAATTCatatggactgtctctgtatagtg-3') and *Xho*I (5'-gataCTCGAGtcagagtctctctcgggctgg-3') restriction sites and subsequently cloned into *Eco*RI/*Xho*I-digested pCMV-Myc vector (Clontech). pcDNA3.1-nNOS [67], pRK5-EGFP-Tau WT and pRK5-EGFP-Tau P301L [27] were kind gifts from Yoichi Osawa (University of Michigan Medical School, Ann Arbor, MI) and Karen Ashe (Addgene plasmid #46904 and #46908; University of Minnesota, Minneapolis, MN), respectively. pcDNA3.1 (Thermo Fisher Scientific) and pEGFP-C3 (Clontech) plasmids were used as empty vector expression controls. All plasmid constructs used in this study were verified by automated DNA sequencing.

Transient transfections and co-immunoprecipitation studies in HEK293T cells: Human embryonic kidney (HEK) 293T cells were obtained from the American Tissue Culture Collection (ATCC; CRL-11268) and cultured as described [68]. Transient transfections with PSD95, nNOS, Tau WT and Tau P301L plasmids were carried out with

Lipofectamine 2000 (Thermo Fisher Scientific) as described by the manufacturer. Experiments were carried out 36hrs later. Cells were lysed in 200µl ice-cold RIPA buffer (50mM Tris.HCl pH8, 150mM NaCl, 1mM EDTA pH8, 1% Igepal CA-630, 0.5% sodium deoxycholate, 0.1% SDS, protease and phosphatase inhibitors). Lysates were sonicated for 10sec on ice with 20% amplitude. A portion of lysate (10µg) was set aside for expression control. For immunoprecipitation studies, 600µg total lysate was incubated overnight at 4°C with either 4µg monoclonal antibody against PSD95 (clone G6G-1C9) or Tau (clone TAU-5; both Thermo Fisher Scientific). Non-specific binding controls were incubated with mouse IgG_{2a} and IgG_1 isotype control antibodies (BioLegend), respectively. On the next day, 30µl Dynabeads Protein G (Thermo Fisher Scientific) was added and incubation was continued by rolling tubes at 4°C for 2hrs. Beads were washed 3 times with RIPA buffer to remove unbound proteins, and then taken up in 30µl SDS-sample buffer. Precipitates were resolved on 4-12% Tris-Glycine protein gels, transferred to PVDF membranes and probed by Western Blotting for the presence of proteins with antibodies against PSD95, Tau and nNOS.

Tau phosphorylation in HEK293T cells: Tau WT and P301L plasmids were transfected and lysates prepared as described above. 20µg total protein was incubated for 1.5hrs at 30°C with 400 units Lambda protein phosphatase (New England Biolabs) in presence of 10mM $MnCl_2$. Companion reactions were treated the same, except for addition of the phosphatase. Tau phosphorylation was assessed by Western Blotting with anti-phospho-Tau antibody clone AT8. Total Tau was detected with Tau5 antibody.

Cognitive testing

Methods for cognitive testing have been described in detail previously [41, 69] and are only summarized. All analyses were performed in a double-blinded fashion.

Barnes maze test: Mice were tested in a group of 10 with the inter-trial interval (20–30 minutes). All of the mice examined were trained with an escape hole located in the same location across trials. No habituation trial was performed. The acquisition phase consisted of 4 consecutive training days with 4 trials per day. After each trial, mice remained in the escape box for 60 seconds before being returned to their home cages. Mice were allowed 3 minutes for each trial to locate the escape hole. On day 5, 24 hr after the last acquisition test, probe trials were performed. Mice were placed in a start quadrant of the Barnes maze and allowed to explore for 90 seconds. Then, we analyzed (a) latency to enter the escape hole during acquisition phase (escape latency) and (b) time spent in escape quadrant in the probe trial.

Y-maze spontaneous alternation behavior: Mice were placed into one of 3 arms of the maze (start arm) and allowed to explore only two of the three arms for 5 min (training trial). The closed arm was opened in the test trial, serving as the novel arm. After a 30-min intertribal interval, the mice were returned to the same start arm and were allowed to explore all three arms for 5 min (test trial). Sessions were video recorded with and analyzed using AnyMaze (San Diego Instruments). Spontaneous alternation was evaluated by scoring the order of entries into each arm during the 5 min of the test trial. Spontaneous alternation (%)

was defined as the ratio of total arm to possible (=total arm alternations minus 2) number of alternations x 100.

Novel object recognition (NOR) test: The test was performed in two consecutive days. On day one, mice were placed in the center of an empty open box and allowed to explore for 5 minutes. On day 2, the mice were placed back to an open box with two identical objects in the center and allowed to explore for 5 minutes. Thirty minutes later, mice were exposed again to a familiar and a novel object, and allowed to explore for 5 minutes. The exploring activity (facing, touching or sniffing the object) was monitored and analyzed using AnyMaze, and the percent of the time spent exploring the novel vs. familiar objects was calculated.

Data analysis

Sample size was determined by power analysis using G*Power (version 3.1.9.2). Experiments were randomized based on the random number generator (www.random.org) and were performed and analyzed in a blinded fashion. Data and Image analysis were done with ImageJ 1.52r (NIH), MATLAB (R2018a, MathWorks, Inc.), or Prism (version 8.3.0, GraphPad Software, Inc.). Data were tested for normal distribution by the D'Agostino-Person test and for outliers by the Grubbs' test (extreme studentized deviate). Two-group comparisons were analyzed by the paired or unpaired two-tailed t-test, as indicated. Multiple comparisons were evaluated by the one-way or (repeated measures) two-way analysis of variance (ANOVA) and Tukey's test. Two photon experiments were analyzed with Mann-Whitney test because the data were not normally distributed. Differences were considered statistically significant for probability values less than 0.05. Data are expressed as means ± SEM.

Reporting Summary.

Further information on research design is available in the Nature Research Reporting Summary linked to this article.

Data availability

All the data supporting conclusions of the current study are presented in the figures. If necessary, the data that support the findings of this study are available from the corresponding authors upon reasonable request. There are no restrictions on data availability.

Code availability

No code was used for the study.

Extended Data

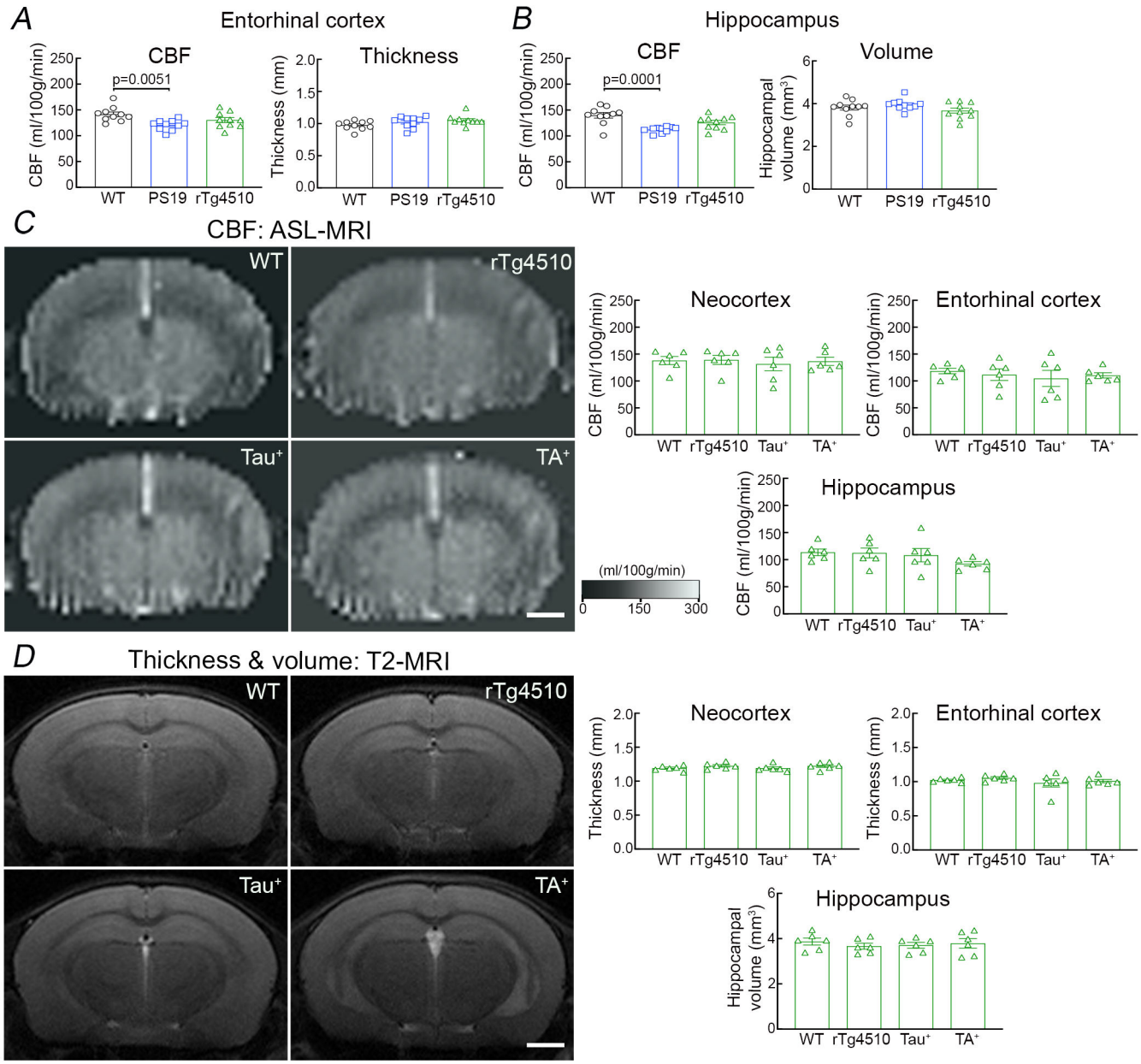

Extended Data Fig. 1. Resting CBF and thickness in PS19, rTg4510, and WT mice at 2-3 months of age

Resting CBF and thickness were bilaterally assessed by ASL- and T2-MRI, respectively, in neocortex, entorhinal cortex, and hippocampus at the bregma level from −1.22 to −1.70 mm. ***A-B.*** A small reduction in entorhinal (***A***) and hippocampal (***B***) CBF is found in PS19 mice and not in rTg4510 mice compared to age-matched WT mice, while entorhinal cortex thickness (***A***) and hippocampal volume (***B***) are comparable in both strains. N=10/group; one-way analysis of variance (ANOVA) with Tukey's test for multiple comparisons. ***C-D.*** Resting CBF (***C***) and thickness (***D***) in the neocortex, entorhinal cortex, and hippocampus are

comparable in rTg4510 mice, expressing both tau (Tau^+) and transactivator (TA^+), and their littermates (WT; Tau^+ only; TA^+ only). Scale bar=1 mm; N=5/group; one-way ANOVA with Tukey's test. Data are presented as mean±SEM. See Source Data 7 for statistical parameters.

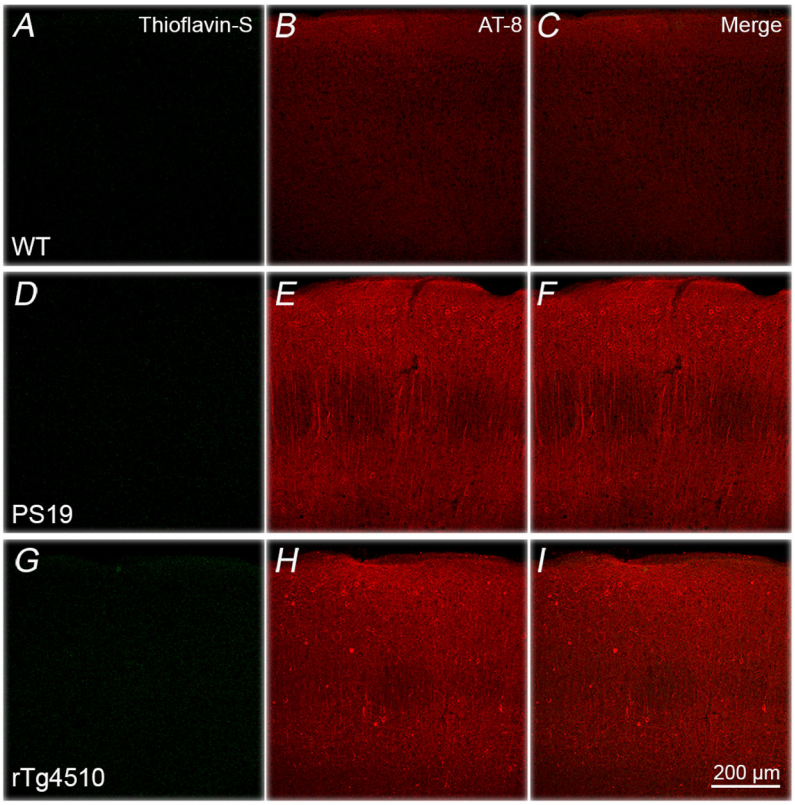

Extended Data Fig. 2. No neurofibrillary tangles are observed in 2-3-month-old PS19, rTg4510, and WT mice

Neurofibrillary tangles, assessed by the thioflavin-S stain, are not observed in the somatosensory cortex of 2-3-month-old WT (***A-C***), PS19 (***D***), and rTg4510 (***G***) mice, but phosphorylated tau (AT-8) is observed in PS19 (***E, F***) and rTg4510 (***H, I***). Images are representative of 3 independent experiments, each including 5 mice/group.

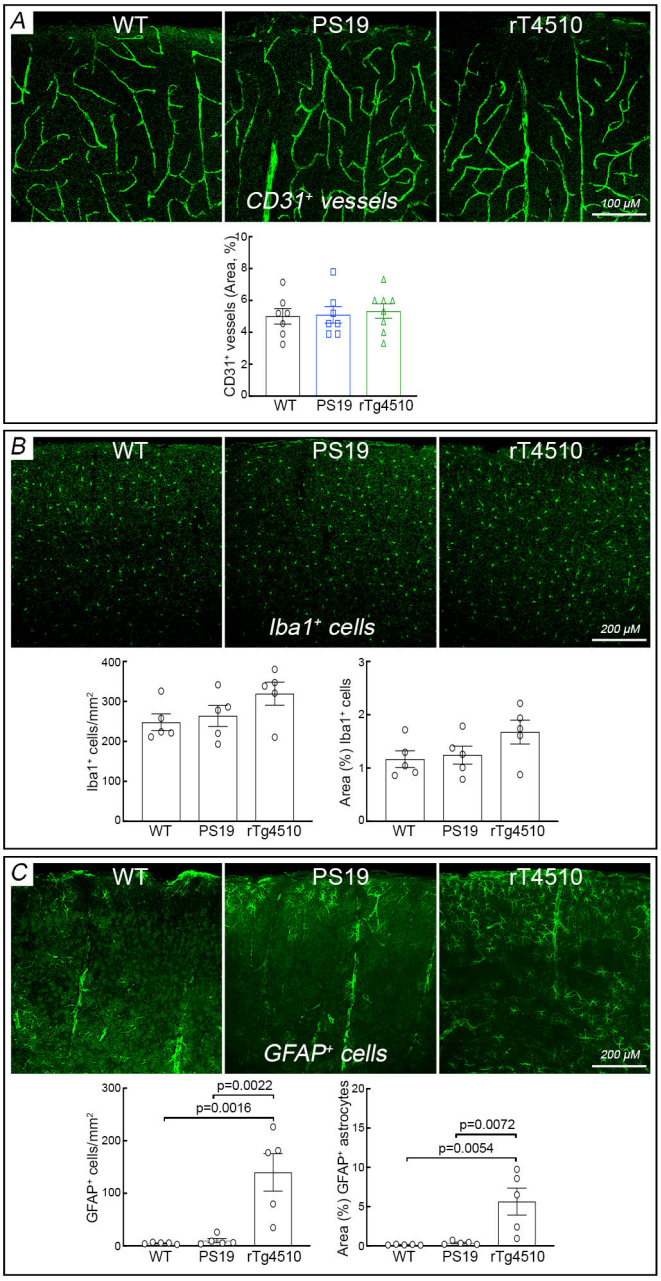

Extended Data Fig. 3. Microvessels, microglia/macrophages, and astrocytes in the neocortex of 2-3-month-old tau mice

Neocortical cluster of differentiation (CD) 31 ($CD31^+$) microvessels (***A***; N=5/group) and $Iba1^+$ microglia/macrophages (***B***; N=5/group) are comparable in PS19, rTg4510, and WT mice at the age of 2-3 months, but enhanced astrogliosis ($GFAP^+$ cells) is found in rTg4510 mice, compared to PS19 and WT mice (***C***; N=5/group). One-way ANOVA and Tukey's test. Data are presented as mean±SEM. See Source Data 8 for statistical parameters.

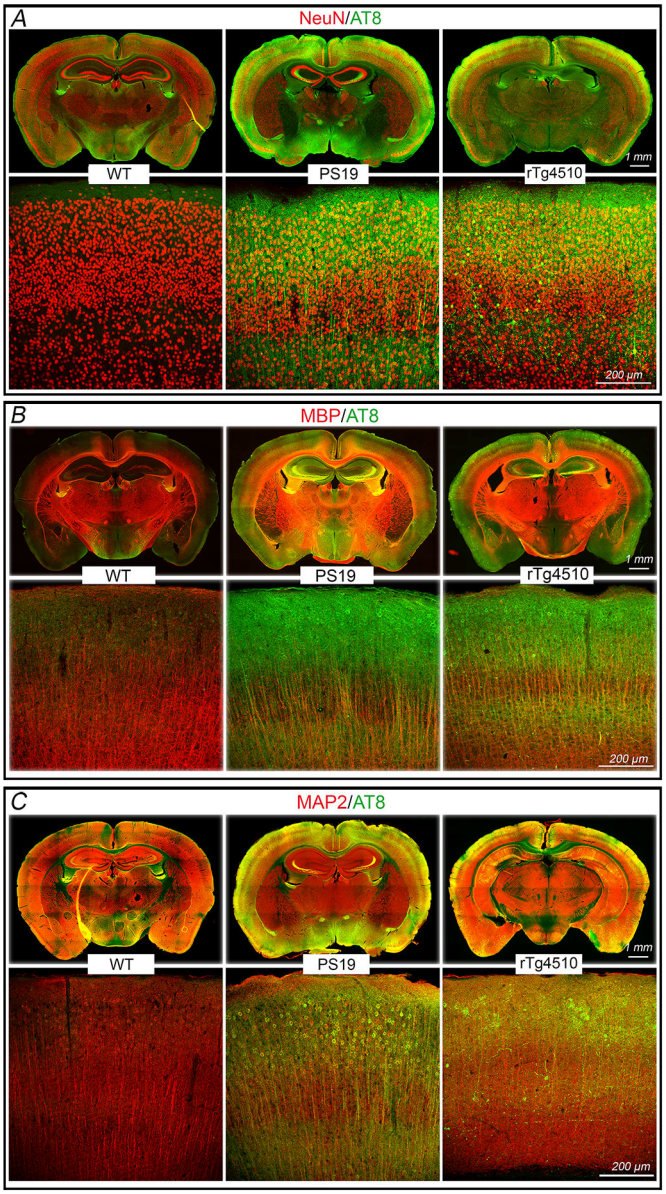

Extended Data Fig. 4. No neuronal loss occurs in PS19 and rTg4510 mice, but mislocalized phosphorylated tau is observed in somatodendritic compartments

The number of neurons ($NeuN^+$) is comparable in PS19, rTg4510, and WT mice (***A***, see quantification in Figure 1C). As anticipated, in PS19 and rTg4510 mice phosphorylated tau ($AT\text{-}8^+$) is co-localized with neurons (NeuN) (***A***) and axons (myelin basic protein, MBP) (***B***). Phosphorylated tau is also observed in dendritic spines (MAP2) (***C***), indicating displacement of tau to somatodendritic compartments. Images are representative of 3 independent experiments, each including 5 mice/group.

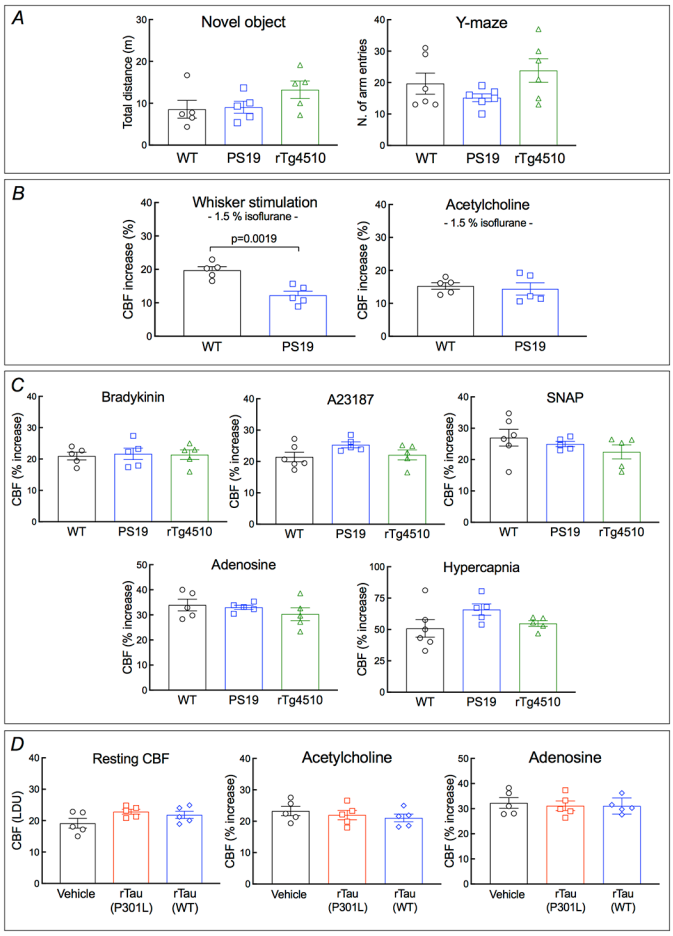

Extended Data Fig. 5. Locomotor activity and neurovascular response in 2-3-month-PS19 and rTg4510 mice

No changes in locomotor activity are observed in novel object recognition and Y-maze tests of rTg4510, compared to WT mice. N=5 for novel object; N=6 for Y-maze. ***B***. The increases in CBF-LDF induced in the whisker barrel cortex by mechanical stimulation of the facial whiskers were markedly attenuated in PS19 mice also under the isoflurane anesthesia regimen used in ASL-MRI studies. N=5/group; two-tailed unpaired t-test. ***C.*** The increases in CBF-LDF produced by the endothelium-dependent (bradykinin or A23187) and -independent (SNAP, adenosine, or hypercapnia) vasodilators are comparable in PS19, rTg4510, and WT mice. N=5/group. ***D.*** Recombinant full-length mutant (2N4R, P301L; 5 μM) or WT (2N4R; 5 μM) tau has no effect on CBF response induced by acetylcholine or adenosine. N=5/group. Data are presented as mean±SEM. One-way ANOVA and Tukey's test.

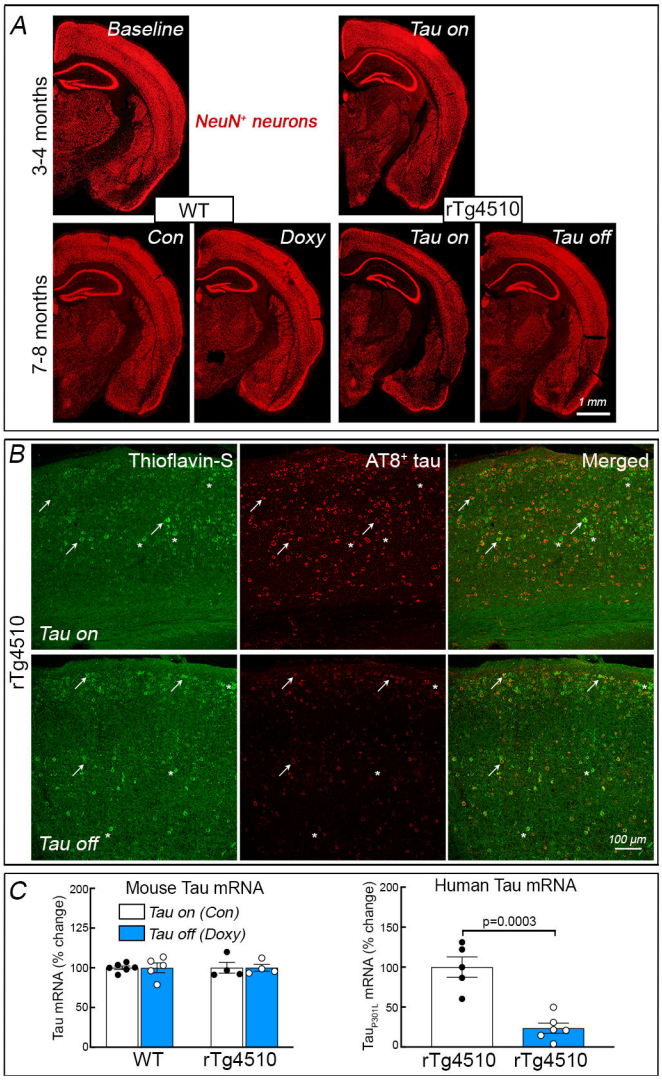

Extended Data Fig. 6. Suppressing tau production with doxycycline reduces P301L tau expression and prevents neuronal loss, tau accumulation in 7-8-month-old rTg4510 mice

A. Doxycycline treatment (*tau off*) for 3-4 months reduces neuronal loss in rTg4510 mice, compared to rTg4510 mice fed control diet (*con* or *tau on*). Treatment with doxycycline (*doxy*) has no effect in WT mice (See Fig. 4C for quantification). ***B***. Suppressing tau production reduces AT-8^{+} tau levels, but not thioflavin-S^{+} neurofibrillary tangles. Arrows indicate co-localization between thioflavin-S^{+} neurofibrillary tangles and AT8^{+} tau, and asterisks denote strong thioflavin-S^{+} neurofibrillary tangles with faint or no AT8^{+} tau. Representative pictures from N=5 mice/group. ***C***. Doxycycline treatment reduces human tau P301L mRNA, but has no effect on mouse tau mRNA. N=5 for WT in mouse tau mRNA and for rTg4510 (tau on) in human tau mRNA; N=4 for rTg4510 in mouse tau mRNA; N=6 for rTg4510 (tau off) in human tau mRNA. Images are representative of 3 independent experiments, each including 5 mice/group. Two-tailed unpaired t-test. Data are presented as mean±SEM.

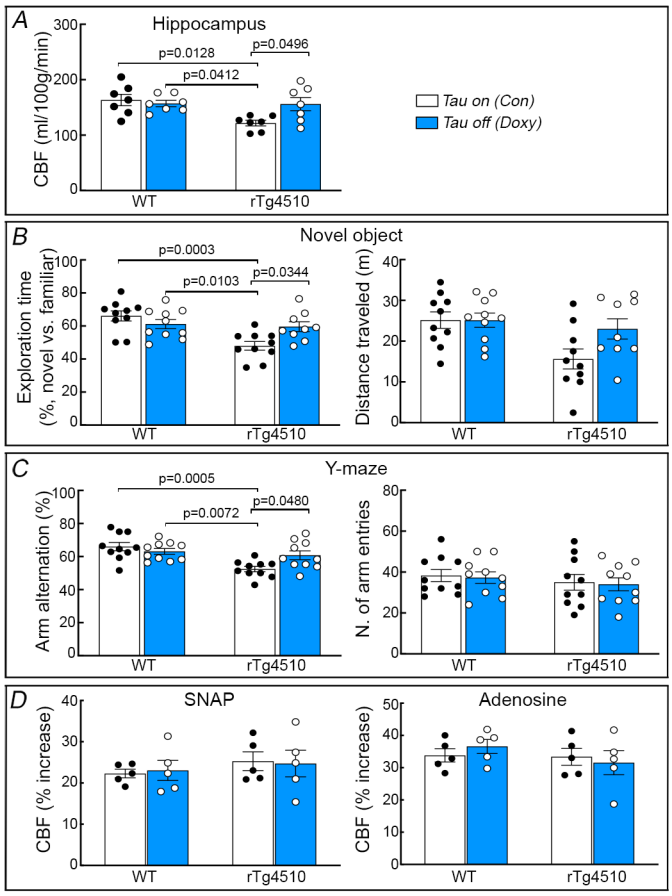

Extended Data Fig. 7. Suppressing tau production with doxycycline prevents cognitive deficits in 7-8-month-old rTg4510 mice

A. Suppressing tau production with doxycycline (*tau off or doxy*), compared with control diet (*tau on or con*), prevents the CBF reduction, assessed by ASL-MRI. N=7/group; two-way ANOVA with Tukey's test. ***B,C.*** Suppressing tau production prevents cognitive deficits, assessed by novel object recognition (***B***; N=10 for WT tau on & off and rTg4510 tau on; N=9 for rTg4510 tau off) and Y-maze test (***C***; N=10/group***),*** but has no effect on locomotor activity, as reflected by distance traveled (***B***) or number of arm entries (***C***). Locomotor activity of rTg4510 mice in the novel object test seems more variable (***B***). Data are presented as mean±SEM. Two-way ANOVA with Tukey's test. ***D***. The CBF increase induced by neocortical superfusion of the NO donor SNAP or adenosine is not altered in 7-8 month-old rTg4510 mice. N=5/group; two-way ANOVA with Tukey's test. Data are presented as mean ±SEM. See Source Data 9 for statistical parameters.

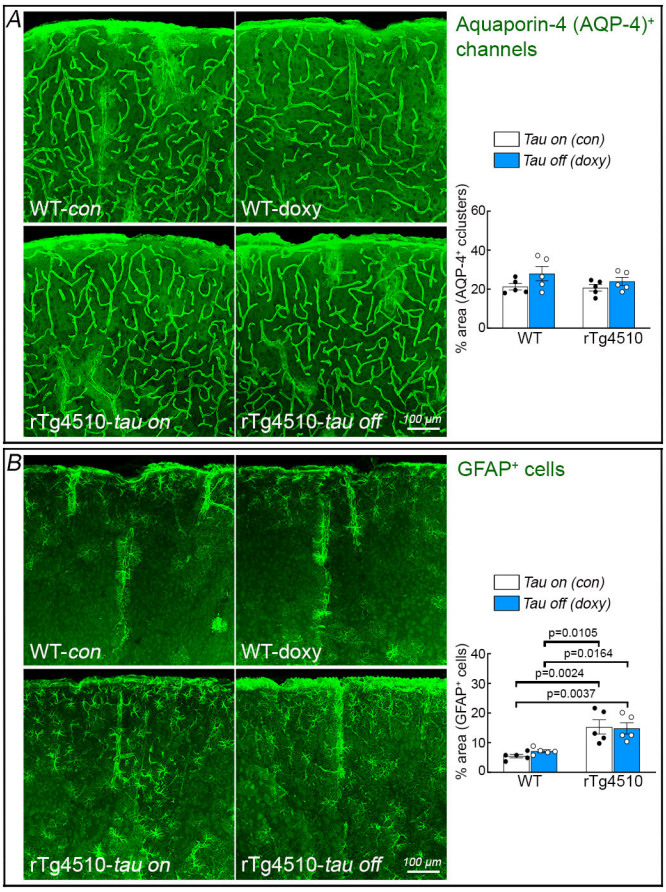

Extended Data Fig. 8. Aquaporin-4 immunoreactivity and astrogliosis are unaffected by suppressing tau production with doxycycline in 7-8-month-old rTg4510 mice

A. AQP-4 immunoreactivity, which labels astrocytic end-feet, was not disrupted in rTg4510 mice with or without doxycycline. N=5/group; two-way ANOVA with Tukey's test; p=0.2420 between WT con & WT doxy, p=0.9985 between WT con & rTg4510 tau on, p=0.8585 between WT con & rTg4510 tau off, p=0.1881 between WT doxy & rTg4510 tau on, p=0.6502 between WT doxy & rTg4510 tau off, and p=0.7804 between rTg4510 tau on & off. Data are presented as mean±SEM. ***B.*** The astrogliosis ($GFAP^+$ cells) observed in rTg4510 mice was not reduced with tau suppression. Data are presented as mean±SEM. N=5/group; two-way ANOVA with Tukey's test. See Source Data 10 for statistical parameters.

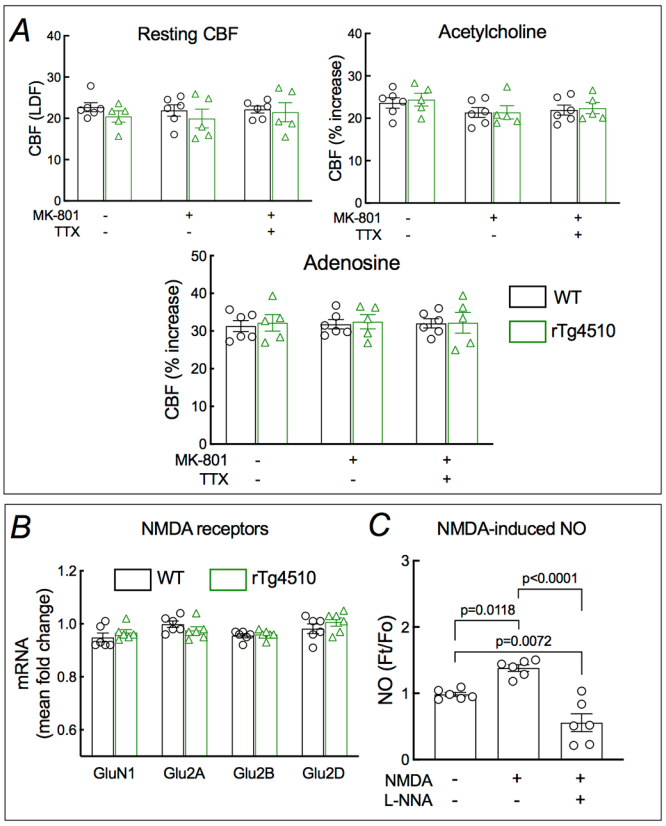

Extended Data Fig. 9. MK-801 and TTX effect on CBF, L-NNA effect on NMDA-induced NO production and expression of NMDA receptor subunits in 2-3-month-old rTg4510 mice

A. MK-801 and/or TTX have no effect on resting CBF or CBF response produced by neocortical superfusion of acetylcholine or adenosine. N=5/group. Data are presented as mean±SEM. ***B***. NMDAR subunits mRNA levels are comparable in WT and rTg4510 mice. N=5/group. Data are presented as mean±SEM. ***C***. Treatment with the NOS inhibitor L-NNA prevents NMDA-induced NO production in isolated cortical neurons from WT mice. Data are presented as mean±SEM. N=6/group; one-way ANOVA with Tukey's test. See Source Data 11 for statistical parameters.

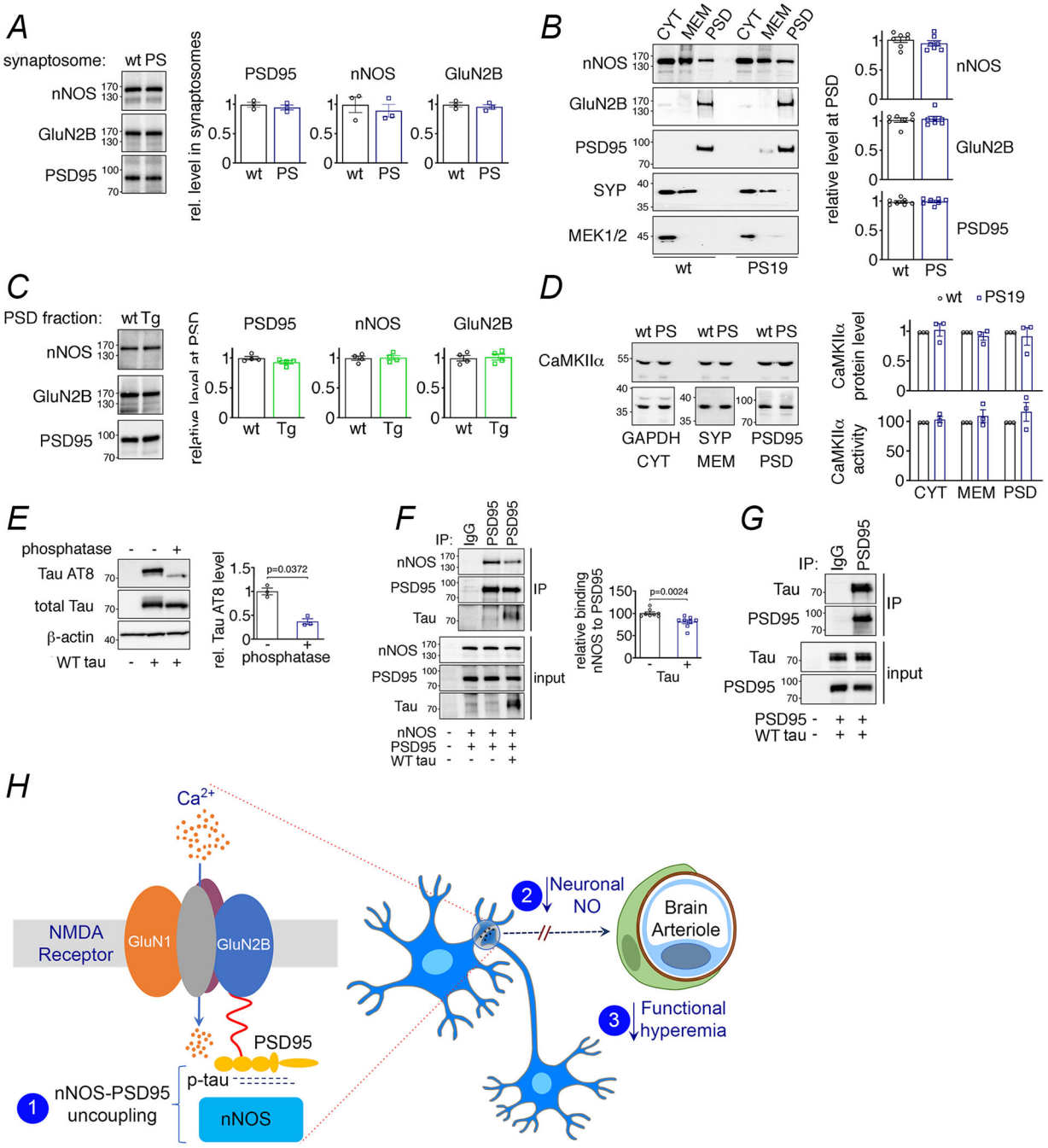

Extended Data Fig. 10. NMDAR-related proteins in PS19 and rTg4510 mice, effects of WT tau on nNOS-PSD95 coupling, and putative mechanisms of the effect of tau on neurovascular function

A-D. Levels and kinase activity of NMDAR-related proteins are not altered in 2-3 month-old PS19 and rTg4510 mice. ***A***. Protein levels of nNOS, GluN2B and PSD95 are unaltered in synaptosomal preparations of PS19 (PS) compared to WT mice. N=3/group. Data are presented as mean±SEM. ***B***. Protein levels of nNOS, GluN2B and PSD95 in PS19 (PS) and WT mice are comparable. The presynaptic marker synaptophysin (SYP) and MEK1/2 were used as membrane (MEM) and cytosolic (CYT) markers, respectively. N=7/group. Data are

presented as mean±SEM. ***C.*** As in PS19 mice, nNOS, GluN2B and PSD95 protein levels are unchanged in PSD preparations of rTg4510 (Tg) mice compared to WT mice. N=4/group. Data are presented as mean±SEM. ***D.*** CaMKIIα level and activity quantified with reference to GAPDH, synaptophysin (SYP), or PSD95 associated with cytoplasm (CYT), membrane (MEM), and/or PSD are not altered in PS19 mice, compared to WT. N=3/group. Data are presented as mean±SEM. Immunoblots in ***A-D*** are cropped; full gel pictures are shown in Source Data 28. ***E-G.*** WT tau impairs binding of nNOS to PSD95 through association with PSD95. ***E.*** WT tau over-expressed in HEK293T cells is susceptible to phosphatase treatment, and thus hyperphosphorylated. N=3/group; unpaired t-test. ***F.*** WT tau co-expression disrupts binding of nNOS to precipitated PSD95. N=8/group; two-tailed unpaired t-test. ***G.*** Exogenously expressed WT tau interacts with PSD95 in HEK293T cells. A representative blot from N=3/group is shown. Data are presented as mean±SEM. Immunoblots in ***E-G*** are cropped; full gel pictures are shown in Source Data 12. ***H.*** Putative mechanism by which tau induces a deficit in neuronal NO and neurovascular dysfunction: pathogenic tau (p-tau) binds to PSD95 and prevents its association with nNOS (1) and the resulting suppression in the NO production evoked by glutamatergic synaptic activity (2) dampens the NO dependent component of the increase in CBF produced by activation (3).

Supplementary Material

Refer to Web version on PubMed Central for supplementary material.

Acknowledgements

Supported by NIH grants R01-NS37853 (CI), R01-NS097805 (LP), R01-NS109588 (KH), Japan Heart Foundation/ Bayer Research Grant Abroad (YH), The Uehara Memorial Foundation Research Fellowship (YH), Japan Society for the Promotion of Science Overseas Research Fellowship (YH), and American Heart Association Postdoctoral Fellowship 20POST35120063 (SJA). We thank Dr. Chris B. Schaffer for helpful suggestions and editing. Support from the Feil Family Foundation is gratefully acknowledged.

References

1. Cummings J, Lee G, Ritter A & Zhong K Alzheimer's disease drug development pipeline: 2018. Alzheimers Dement (N Y) 4, 195–214 (2018). [PubMed: 29955663]
2. Henstridge CM, Hyman BT & Spires-Jones TL Beyond the neuron-cellular interactions early in Alzheimer disease pathogenesis. Nat Rev Neurosci 20, 94–108 (2019). [PubMed: 30643230]
3. Knopman DS Lowering of Amyloid-Beta by beta-Secretase Inhibitors - Some Informative Failures. N Engl J Med 380, 1476–1478 (2019). [PubMed: 30970194]
4. Boyle PA, et al. Attributable risk of Alzheimer's dementia attributed to age-related neuropathologies. Ann Neurol 85, 114–124 (2019). [PubMed: 30421454]
5. Iadecola C & Gottesman RF Cerebrovascular Alterations in Alzheimer Disease. Circ Res 123, 406–408 (2018). [PubMed: 30355253]
6. Iturria-Medina Y, et al. Early role of vascular dysregulation on late-onset Alzheimer's disease based on multifactorial data-driven analysis. Nat Commun 7, 11934 (2016). [PubMed: 27327500]
7. Rabin JS, et al. Vascular Risk and beta-Amyloid Are Synergistically Associated with Cortical Tau. Ann Neurol 85, 272–279 (2019). [PubMed: 30565287]
8. Iadecola C The Neurovascular Unit Coming of Age: A Journey through Neurovascular Coupling in Health and Disease. Neuron 96, 17–42 (2017). [PubMed: 28957666]
9. Scheltens P, et al. Alzheimer's disease. Lancet 388, 505–517 (2016). [PubMed: 26921134]

10. Dopper EG, et al. Cerebral blood flow in presymptomatic MAPT and GRN mutation carriers: A longitudinal arterial spin labeling study. Neuroimage Clin 12, 460–465 (2016). [PubMed: 27625986]
11. Kurata T, et al. PSP as distinguished from CBD, MSA-P and PD by clinical and imaging differences at an early stage. Intern Med 50, 2775–2781 (2011). [PubMed: 22082889]
12. Lunau L, et al. Presymptomatic cerebral blood flow changes in CHMP2B mutation carriers of familial frontotemporal dementia (FTD-3), measured with MRI. BMJ Open 2, e000368 (2012).
13. Iadecola C The pathobiology of vascular dementia. Neuron 80, 844–866 (2013). [PubMed: 24267647]
14. Sweeney MD, Kisler K, Montagne A, Toga AW & Zlokovic BV The role of brain vasculature in neurodegenerative disorders. Nat Neurosci 21, 1318–1331 (2018). [PubMed: 30250261]
15. Brenman JE, et al. Interaction of nitric oxide synthase with the postsynaptic density protein PSD-95 and alpha1-syntrophin mediated by PDZ domains. Cell 84, 757–767 (1996). [PubMed: 8625413]
16. Christopherson KS, Hillier BJ, Lim WA & Bredt DS PSD-95 assembles a ternary complex with the N-methyl-D-aspartic acid receptor and a bivalent neuronal NO synthase PDZ domain. J Biol Chem 274, 27467–27473 (1999). [PubMed: 10488080]
17. Kornau HC, Schenker LT, Kennedy MB & Seeburg PH Domain interaction between NMDA receptor subunits and the postsynaptic density protein PSD-95. Science 269, 1737–1740 (1995). [PubMed: 7569905]
18. Girouard H, et al. NMDA receptor activation increases free radical production through nitric oxide and NOX2. J Neurosci 29, 2545–2552 (2009). [PubMed: 19244529]
19. Mishra A, et al. Astrocytes mediate neurovascular signaling to capillary pericytes but not to arterioles. Nat Neurosci 19, 1619–1627 (2016). [PubMed: 27775719]
20. Park L, et al. Key role of tissue plasminogen activator in neurovascular coupling. Proc Natl Acad Sci U S A 105, 1073–1078 (2008). [PubMed: 18195371]
21. Bennett RE, et al. Tau induces blood vessel abnormalities and angiogenesis-related gene expression in P301L transgenic mice and human Alzheimer's disease. Proc Natl Acad Sci U S A 115, E1289–E1298 (2018). [PubMed: 29358399]
22. Blair LJ, et al. Tau depletion prevents progressive blood-brain barrier damage in a mouse model of tauopathy. Acta Neuropathol Commun 3, 8 (2015). [PubMed: 25775028]
23. Ittner A & Ittner LM Dendritic Tau in Alzheimer's Disease. Neuron 99, 13–27 (2018). [PubMed: 30001506]
24. Mondragon-Rodriguez S, et al. Interaction of endogenous tau protein with synaptic proteins is regulated by N-methyl-D-aspartate receptor-dependent tau phosphorylation. J Biol Chem 287, 32040–32053 (2012). [PubMed: 22833681]
25. Yoshiyama Y, et al. Synapse loss and microglial activation precede tangles in a P301S tauopathy mouse model. Neuron 53, 337–351 (2007). [PubMed: 17270732]
26. Santacruz K, et al. Tau suppression in a neurodegenerative mouse model improves memory function. Science 309, 476–481 (2005). [PubMed: 16020737]
27. Hoover BR, et al. Tau mislocalization to dendritic spines mediates synaptic dysfunction independently of neurodegeneration. Neuron 68, 1067–1081 (2010). [PubMed: 21172610]
28. Ramsden M, et al. Age-dependent neurofibrillary tangle formation, neuron loss, and memory impairment in a mouse model of human tauopathy (P301L). J Neurosci 25, 10637–10647 (2005). [PubMed: 16291936]
29. Niwa K, Haensel C, Ross ME & Iadecola C Cyclooxygenase-1 participates in selected vasodilator responses of the cerebral circulation. Circ Res 88, 600–608 (2001). [PubMed: 11282894]
30. Iadecola C Does nitric oxide mediate the increases in cerebral blood flow elicited by hypercapnia? Proc Natl Acad Sci U S A 89, 3913–3916 (1992). [PubMed: 1570313]
31. Iadecola C, Pelligrino DA, Moskowitz MA & Lassen NA Nitric oxide synthase inhibition and cerebrovascular regulation. J Cereb Blood Flow Metab 14, 175–192 (1994). [PubMed: 7509338]
32. Uekawa K, et al. Obligatory Role of EP1 Receptors in the Increase in Cerebral Blood Flow Produced by Hypercapnia in the Mice. PLoS One 11, e0163329 (2016). [PubMed: 27657726]

33. Fa M, et al. Extracellular Tau Oligomers Produce An Immediate Impairment of LTP and Memory. Sci Rep 6, 19393 (2016). [PubMed: 26786552]
34. Yamada K, et al. In vivo microdialysis reveals age-dependent decrease of brain interstitial fluid tau levels in P301S human tau transgenic mice. J Neurosci 31, 13110–13117 (2011). [PubMed: 21917794]
35. Brochner CB, Holst CB & Mollgard K Outer brain barriers in rat and human development. Front Neurosci 9, 75 (2015). [PubMed: 25852456]
36. Sykova E Diffusion properties of the brain in health and disease. Neurochem Int 45, 453–466 (2004). [PubMed: 15186911]
37. Chen BR, Kozberg MG, Bouchard MB, Shaik MA & Hillman EM A critical role for the vascular endothelium in functional neurovascular coupling in the brain. J Am Heart Assoc 3, e000787 (2014). [PubMed: 24926076]
38. Longden TA, et al. Capillary K(+)-sensing initiates retrograde hyperpolarization to increase local cerebral blood flow. Nat Neurosci 20, 717–726 (2017). [PubMed: 28319610]
39. Lecrux C, et al. Pyramidal neurons are "neurogenic hubs" in the neurovascular coupling response to whisker stimulation. J Neurosci 31, 9836–9847 (2011). [PubMed: 21734275]
40. Buerk DG, Ances BM, Greenberg JH & Detre JA Temporal dynamics of brain tissue nitric oxide during functional forepaw stimulation in rats. Neuroimage 18, 1–9 (2003). [PubMed: 12507439]
41. Koizumi K, et al. Apoepsilon4 disrupts neurovascular regulation and undermines white matter integrity and cognitive function. Nat Commun 9, 3816 (2018). [PubMed: 30232327]
42. Sattler R, et al. Specific coupling of NMDA receptor activation to nitric oxide neurotoxicity by PSD-95 protein. Science 284, 1845–1848 (1999). [PubMed: 10364559]
43. Kopeikina KJ, et al. Synaptic alterations in the rTg4510 mouse model of tauopathy. J Comp Neurol 521, 1334–1353 (2013). [PubMed: 23047530]
44. Warmus BA, et al. Tau-mediated NMDA receptor impairment underlies dysfunction of a selectively vulnerable network in a mouse model of frontotemporal dementia. J Neurosci 34, 16482–16495 (2014). [PubMed: 25471585]
45. Gamache J, et al. Factors other than hTau overexpression that contribute to tauopathy-like phenotype in rTg4510 mice. Nat Commun 10, 2479 (2019). [PubMed: 31171783]
46. Goodwin LO, et al. Large-scale discovery of mouse transgenic integration sites reveals frequent structural variation and insertional mutagenesis. Genome Res 29, 494–505 (2019). [PubMed: 30659012]
47. Hardingham N, Dachtler J & Fox K The role of nitric oxide in pre-synaptic plasticity and homeostasis. Front Cell Neurosci 7, 190 (2013). [PubMed: 24198758]
48. Garthwaite J NO as a multimodal transmitter in the brain: discovery and current status. Br J Pharmacol 176, 197–211 (2019). [PubMed: 30399649]
49. Zhu J, Shang Y & Zhang M Mechanistic basis of MAGUK-organized complexes in synaptic development and signalling. Nat Rev Neurosci 17, 209–223 (2016). [PubMed: 26988743]

Method-only References

50. Karp NA, et al. Applying the ARRIVE Guidelines to an In Vivo Database. PLoS Biol 13, e1002151 (2015). [PubMed: 25992600]
51. Franklin KBJ & Paxinos G The mouse brain in stereotaxic coordinates (Academic Press, 1997).
52. Jackman K, et al. Progranulin deficiency promotes post-ischemic blood-brain barrier disruption. J Neurosci 33, 19579–19589 (2013). [PubMed: 24336722]
53. Park L, et al. Age-dependent neurovascular dysfunction and damage in a mouse model of cerebral amyloid angiopathy. Stroke 45, 1815–1821 (2014). [PubMed: 24781082]
54. Park L, et al. The key role of transient receptor potential melastatin-2 channels in amyloid-beta-induced neurovascular dysfunction. Nat Commun 5, 5318 (2014). [PubMed: 25351853]
55. Iadecola C Nitric oxide participates in the cerebrovasodilation elicited from cerebellar fastigial nucleus. Am J Physiol 263, R1156–1161 (1992). [PubMed: 1443234]

56. Park L, et al. Scavenger receptor CD36 is essential for the cerebrovascular oxidative stress and neurovascular dysfunction induced by amyloid-beta. Proc Natl Acad Sci U S A 108, 5063–5068 (2011). [PubMed: 21383152]
57. Cruz Hernandez JC, et al. Neutrophil adhesion in brain capillaries reduces cortical blood flow and impairs memory function in Alzheimer's disease mouse models. Nat Neurosci 22, 413–420 (2019). [PubMed: 30742116]
58. Shih AY, Mateo C, Drew PJ, Tsai PS & Kleinfeld D A polished and reinforced thinned-skull window for long-term imaging of the mouse brain. J Vis Exp (2012).
59. Dunn AK, Bolay H, Moskowitz MA & Boas DA Dynamic imaging of cerebral blood flow using laser speckle. J Cereb Blood Flow Metab 21, 195–201 (2001). [PubMed: 11295873]
60. Park L, et al. Exogenous NADPH increases cerebral blood flow through NADPH oxidase-dependent and -independent mechanisms. Arterioscler Thromb Vasc Biol 24, 1860–1865 (2004). [PubMed: 15308559]
61. Kazama K, Wang G, Frys K, Anrather J & Iadecola C Angiotensin II attenuates functional hyperemia in the mouse somatosensory cortex. Am J Physiol Heart Circ Physiol 285, H1890–1899 (2003). [PubMed: 12907423]
62. Coleman CG, et al. Chronic intermittent hypoxia induces NMDA receptor-dependent plasticity and suppresses nitric oxide signaling in the mouse hypothalamic paraventricular nucleus. J Neurosci 30, 12103–12112 (2010). [PubMed: 20826673]
63. Wang G, et al. Angiotensin II slow-pressor hypertension enhances NMDA currents and NOX2-dependent superoxide production in hypothalamic paraventricular neurons. Am J Physiol Regul Integr Comp Physiol 304, R1096–1106 (2013). [PubMed: 23576605]
64. Kawano T, et al. Prostaglandin E2 EP1 receptors: downstream effectors of COX-2 neurotoxicity. Nat Med 12, 225–229 (2006). [PubMed: 16432513]
65. Machida S, et al. Cycloamylose as an efficient artificial chaperone for protein refolding. FEBS Lett 486, 131–135 (2000). [PubMed: 11113453]
66. Ittner LM, et al. Dendritic function of tau mediates amyloid-beta toxicity in Alzheimer's disease mouse models. Cell 142, 387–397 (2010). [PubMed: 20655099]
67. Peng HM, Morishima Y, Pratt WB & Osawa Y Modulation of heme/substrate binding cleft of neuronal nitric-oxide synthase (nNOS) regulates binding of Hsp90 and Hsp70 proteins and nNOS ubiquitination. J Biol Chem 287, 1556–1565 (2012). [PubMed: 22128174]
68. Hochrainer K, et al. The ubiquitin ligase HERC3 attenuates NF-kappaB-dependent transcription independently of its enzymatic activity by delivering the RelA subunit for degradation. Nucleic Acids Res 43, 9889–9904 (2015). [PubMed: 26476452]
69. Faraco G, et al. Perivascular macrophages mediate the neurovascular and cognitive dysfunction associated with hypertension. J Clin Invest 126, 4674–4689 (2016). [PubMed: 27841763]

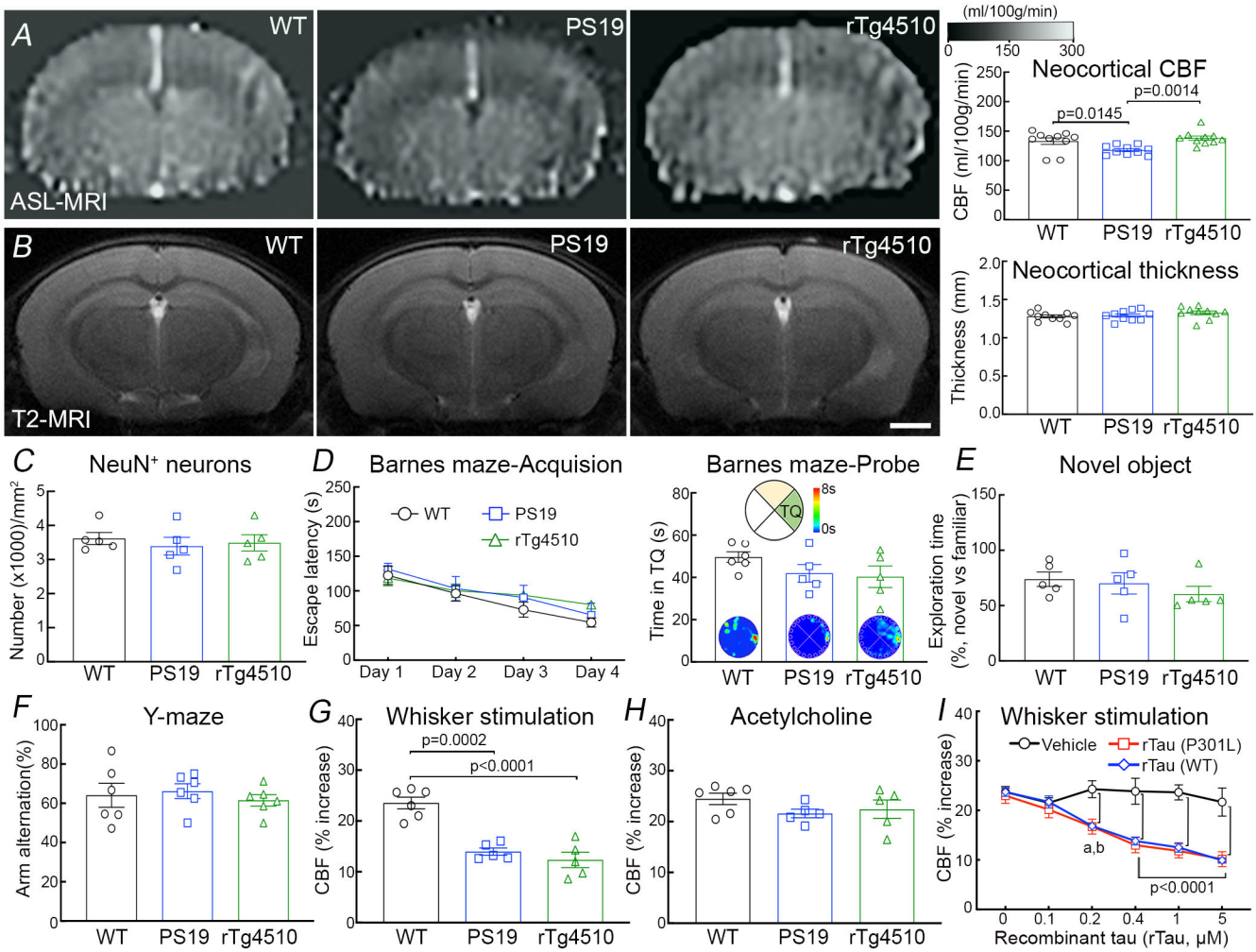

Figure 1: Neurovascular coupling is selectively disrupted in tau mice prior to tau pathology and cognitive impairment.

A. Neocortical CBF, assessed by ASL-MRI, shows no reduction in 2-3-month-old rTg4510 and small reduction in 2-3-month-old PS19 mice, compared to age-matched WT mice. N=10/group; one-way analysis of variance (ANOVA) with Tukey's test for multiple comparisons. ***B.*** Neocortical thickness, assessed bilaterally in T2-weighted MRI images at the level of the somatosensory cortex (−1.22 to −1.70 from bregma), is comparable in PS19, rTg4510, and WT mice. Scale bar=1 mm. N=10/group. ***C.*** The number of neurons ($NeuN^+$) does not differ in PS19, rTg4510, and WT mice. N=5/group (see also Extended data Figure 4A). ***D-F.*** No cognitive impairment is observed at the Barnes maze test (***D***), novel object recognition (***E***), or Y-maze test (***F***). N=5/group. ***G-H***. The increases in CBF induced in the whisker barrel cortex by mechanical stimulation of the facial whiskers (***G***; N=5/group; one-way ANOVA with Tukey's test), but not by neocortical superfusion of acetylcholine (***H***), is markedly attenuated both in PS19 and rTg4510 mice, compared to WT mice. ***I***. Neocortical superfusion of recombinant tau (WT tau or P301L mutant) attenuates the increase in CBF evoked by whisker stimulation in a dose-dependent manner. N=5/group; one-way ANOVA

with Tukey's test between groups at each doses. Data are presented as mean±SEM. See Source Data 1 for statistical parameters.

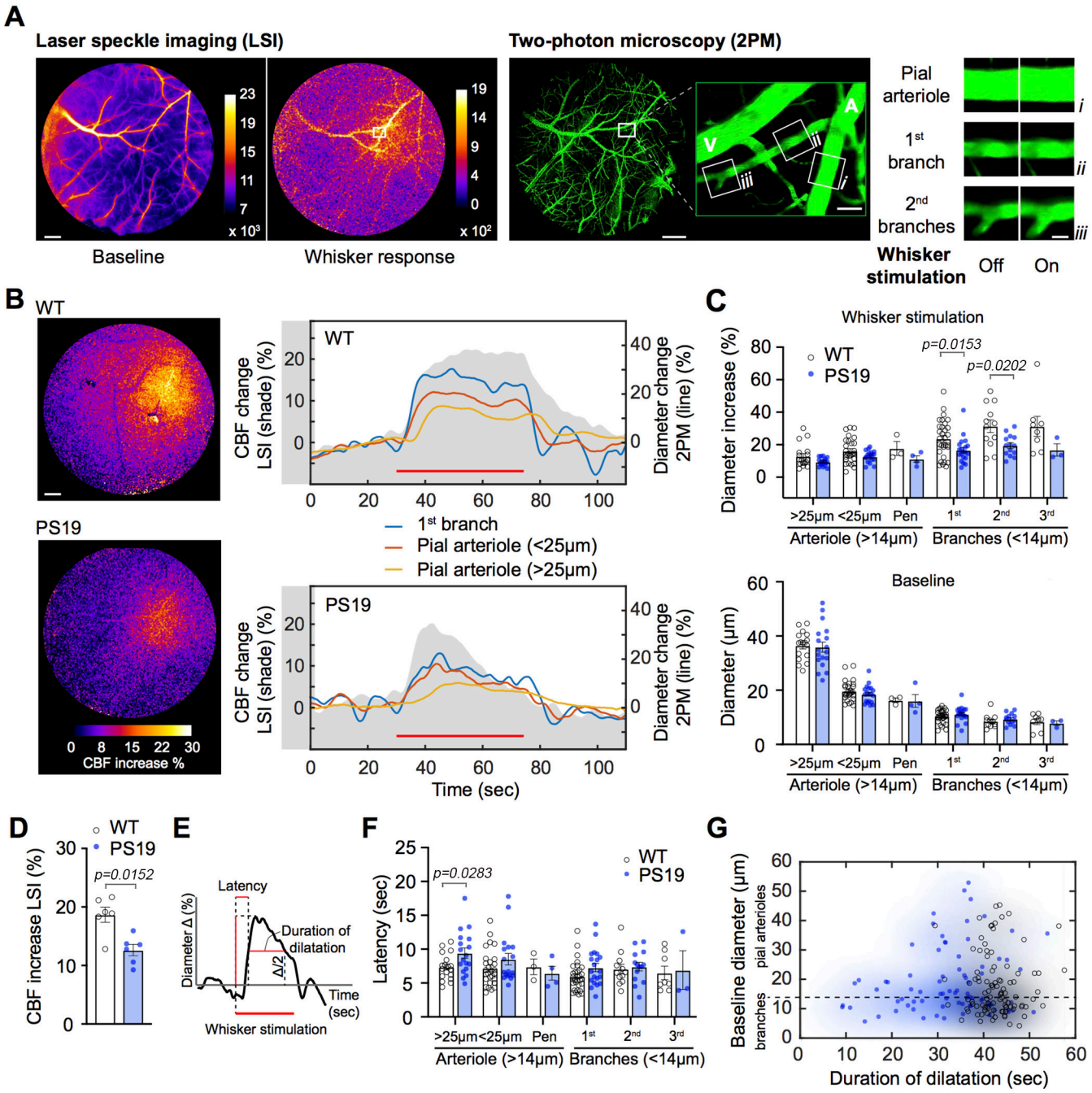

Figure 2: Suppression of neurovascular coupling in tau mice results from impaired vasodilatation of intracerebral arterioles.

A. Protocol used to examine neurovascular coupling with laser speckle imager (LSI) and two-photon microscopy (2PM) in 2-3 months old PS19 mice. LSI images of neocortical surface vasculature were used to identify the microvasculature in the barrel cortex at baseline and during whisker stimulation (left panels), and to select candidate vessels to examine the neurovascular coupling under 2PM. 2PM images of the microvasculature identified by LSI (right panels). The microvessel segments (i, ii, & iii) examined are shown in the enlargement of the area in the white square. Examples of diameter changes induced by

whisker stimulation (off: baseline; on: whisker stimulation) in the microvascular segments studied (i, ii, & iii). Scale bars from the left: 500, 500, 100, and 20 μm, respectively. A, artery; V, vein. ***B.*** The left panel shows the LSI signal increase (% change) induced by whisker stimulation in WT (top) and PS19 mice (bottom). Scale bar=500 μm. The right panel shows the changes in LSI signal (shaded gray area) and in microvascular segment diameter (colored lines) evoked by whisker stimulation in WT (top) and PS19 (bottom) mice. In ***A*** and ***B***, laser-speckle images are representative of 5 independent experiments per group. ***C.*** Diameter changes induced by whisker stimulation (top; %) and baseline diameter (bottom; μm) in microvessels of different sizes in WT and PS19 mice (N=5/group). Multiple measurements were taken for each mouse and values were binned for vessel size and branch number; two-tailed Mann-Whitney test. Arterioles >14μm refer to pial (<25μm or >25mμ) or penetrating (pen) arterioles. Branches (<14μm) are from both pial and penetrating arterioles. ***D.*** Peak increase in CBF evoked by whisker stimulation, recorded with LSI, are attenuated in PS19, compared to WT mice. N=6/group; two-tailed unpaired t-test. ***E-G.*** Quantification of the latency and duration of the microvascular diameter changes induced by whisker stimulation. Representative trace of the % increase in CBF evoked by whisker stimulation indicating how latency and duration of CBF increase were measured (**E**). The latency, presented in **F** (n=5/group), is determined as time to half-positive maximum during whisker stimulation, and the duration, presented in **G** (n=5/group), as time of the CBF increase above half-positive maximum. See panel **C** for description of arterioles and branches. Multiple measurements were taken for each mouse and values were binned for vessel size and branch number; two-tailed Mann-Whitney test. In ***G***, shaded in blue are PS19 (closed blue circles) and in black WT mice (open black circles); Data are presented as mean±SEM.

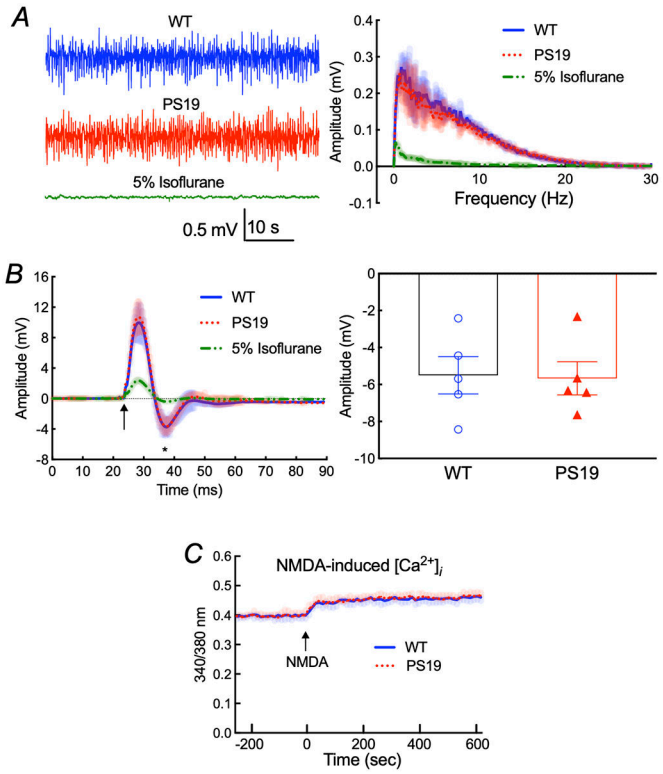

Figure 3: Spontaneous and evoked neural activity and NMDA-induced Ca^{2+} increase are not altered in PS19 mice.

A. The amplitude and frequency distribution of neocortical electrical activity in 2-3 month-old PS19 and age-matched WT mice are comparable. As a positive control, treatment with 5% isoflurane completely abolishes the cortical neural activity. N=5/group. ***B***. The field potentials evoked by electrical stimulation of the whisker pad are comparable in PS19 and WT mice. The arrow indicates the application of the stimulus. The amplitude of the negative wave of the field potentials (asterisk) does not differ (p=0.9050) between PS19 and WT mice. N=5/group; two-tailed unpaired t-test. ***C***. The NMDA-induced increase in intracellular Ca^{2+} assessed in dissociated neocortical neurons of 2-3-month-old PS19 mice by Fura2 imaging is not altered, compared to WT mice. N=5/group. Shading indicates SEM. Data are presented as mean±SEM.

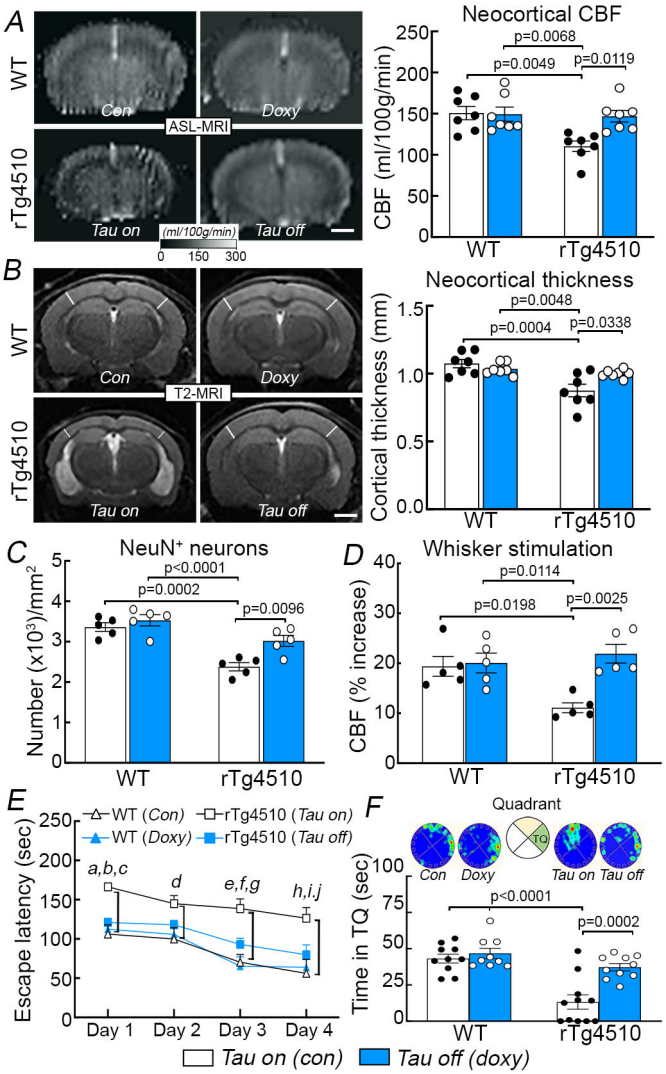

Figure 4: Suppressing tau production rescues neurovascular coupling and prevents cortical atrophy and cognitive deficits in older rTg4510 mice.

Suppressing tau production in 7-8 month-old rTg4510 mice with doxycycline in the diet (*doxy* or *tau off*), compared to age-matched rTg4510 treated with control diet (*con* or *tau on*), restores resting neocortical CBF assessed by ASL-MRI (***A***; N=7/group), neocortical thickness examined by T2 MRI (***B***; N=7/group), and neuronal loss ($NeuN^+$) (***C***; N=7/group) (see also Extended data Figure 6B). Turning down tau also preserves CBF response to whisker stimulation (***D***; N=5/group) and spatial memory assessed by Barnes maze acquisition test (***E***; N=10/group) and probe test (***F***; N=10/group). In ***E***, *a, p*=0.0341 vs rTg4510 (*Tau off*); *b, p*=0.0021 vs WT (*Con*); *c, p*=0.0101 vs WT (*Doxy*); *d, p*=0.0363 vs WT (*Con*); *e, p*=0.0331 vs rTg4510 (*Tau off*); *f, p*=0.0004 vs WT (*Con*); *g, p*=0.0002 vs WT (*Doxy*); *h, p*=0.0294 vs rTg4510 (*Tau off*); *I, p*=0.0002 vs WT (*Con*); *j, p*=0.0019 vs WT (*Doxy*). Data in ***A-D*** and ***F*** are analyzed by two-way ANOVA with Tukey's test and data in ***E*** by repeated measures two-way ANOVA with Tukey's test. Data are presented as mean ±SEM. See Source Data 2 for statistical parameters.

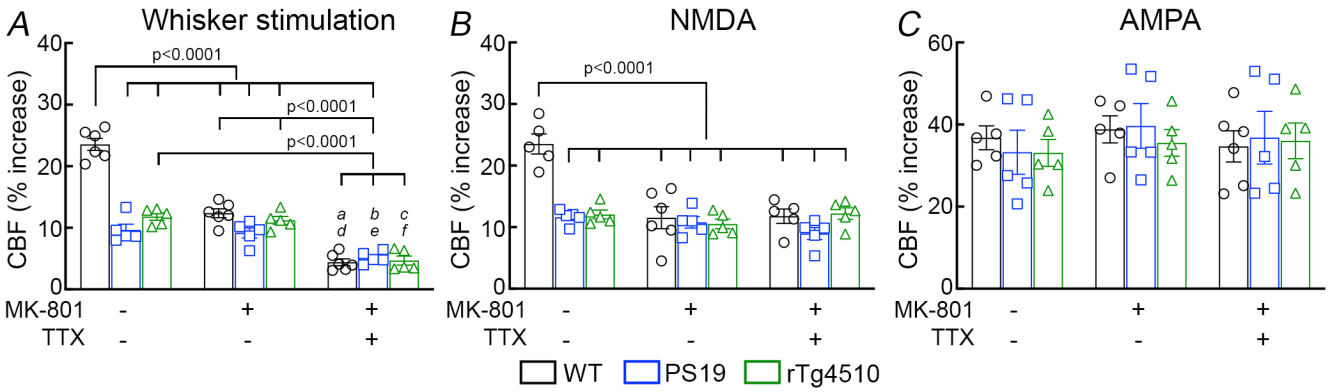

Figure 5: The NMDA-dependent component of functional hyperemia is selectively suppressed in tau mice.

A. Neocortical superfusion with the NMDAR antagonist MK-801 (10 μM) attenuates the CBF increase evoked by whisker stimulation in 2-3 months old WT and not in PS19 and rTg4510 mice, whereas superfusion with the Na^+ channel blocker TTX (3 μM) attenuates the response in all groups. *a*=0.0003, *b*=0.0055, and *c*=0.0015 vs PS19 no treatment; *d*=0.0014, *e*=0.0180, and *f*=0.0052 vs PS19 MK-801; N=6 for WT in whisker stimulation; N=5 for the rest; two-way ANOVA and Tukey's test. ***B.*** The increase in CBF produced by topical application of NMDA (40 μM) is attenuated in PS19 and rTg4510, compared to WT mice. MK-801 attenuates the CBF increase in WT, but not in PS19 and rTg4510 mice. TTX has no effects both in both WT and rTg4510 mice. N=5/group; two-way ANOVA and Tukey's test. ***C***. The CBF increase produced by topical application of AMPA (10 μM) is comparable in WT, PS19, and rTg4510 mice, and is not affected by MK-801 or TTX. N=6 for MK-801- & TTX-treated WT in AMPA; N=5 for the rest. Data are presented as mean ±SEM. See Source Data 3 for statistical parameters.

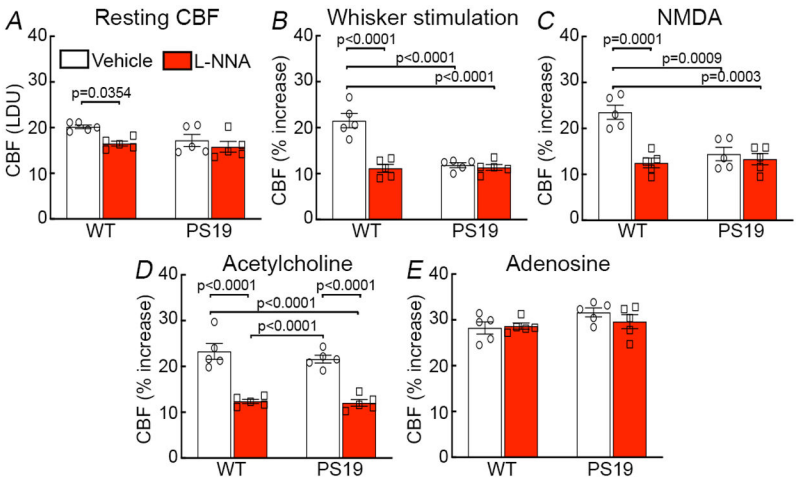

Figure 6: The NO-dependent component of functional hyperemia is attenuated in tau mice.

Topical application of broad-spectrum NOS inhibitor L-nitroarginine (L-NNA, 1 mM) attenuates resting CBF (***A***), the increase in CBF produced by whisker stimulation (***B***) or by neocortical application of NMDA (40 μM; ***C***) in 2-3 months old WT, but not in age-matched PS19 mice. L-NNA attenuates the CBF increase induced by neocortical application of acetylcholine (10 μM) both in WT and PS19 mice (***D***), but has no effect on the response to adenosine (***E;*** p=0.2121 between WT and PS19 no treatment; p=0.9951 between WT no treatment and WT L-NNA; p=0.8398 between WT no treatment and PS19 L-NNA; p=3048 between PS19 no treatment and WT L-NNA; p=0.6245 between PS19 no treatment and PS19 L-NNA; p=0.9333 between WT L-NNA and PS19 L-NNA). N=5/group; two-way ANOVA and Tukey's test. Data are presented as mean±SEM. See Source Data 4 for statistical parameters.

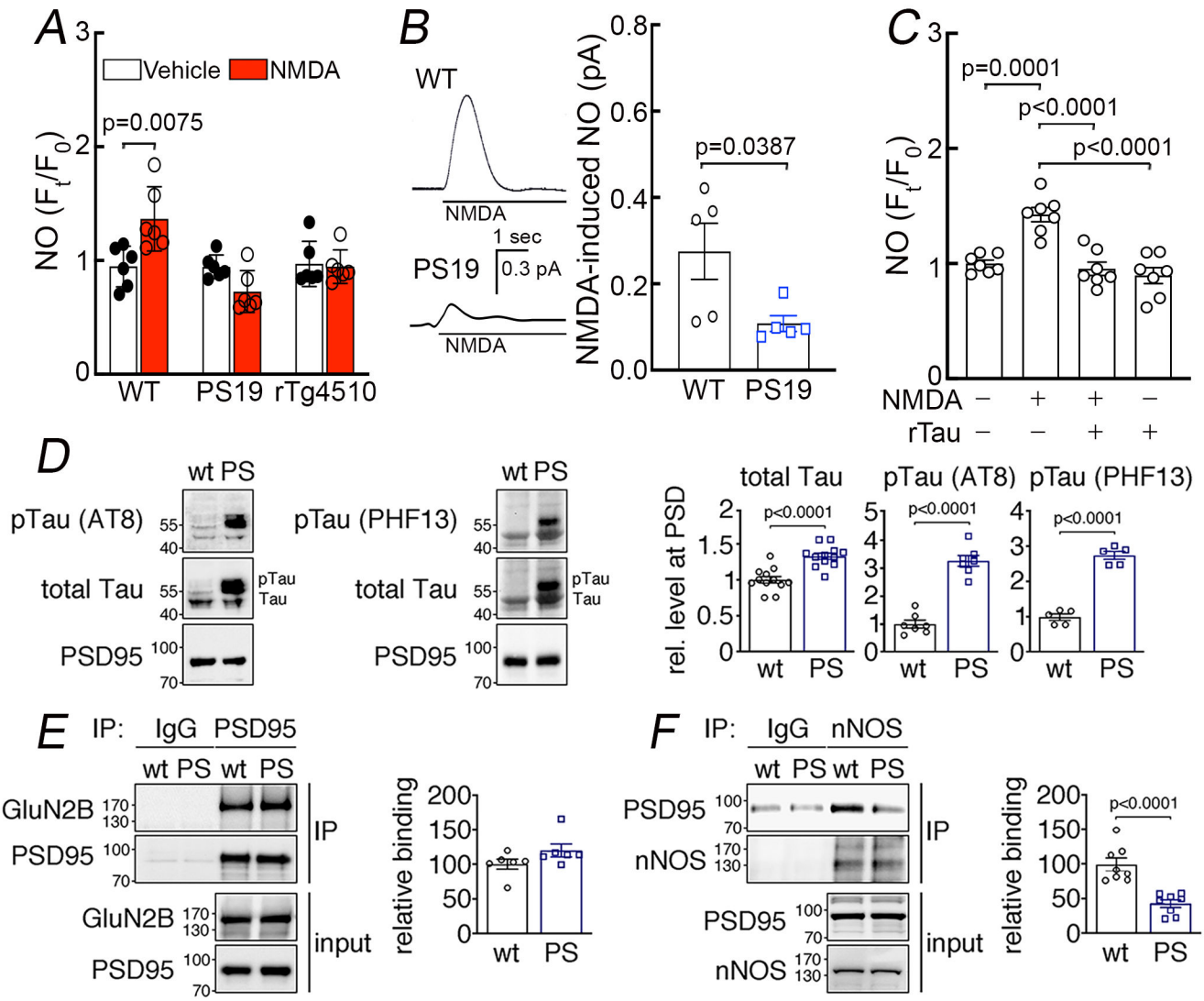

Figure 7: Suppression of NMDAR-induced neuronal NO production and dissociation of nNOS from PSD95 in tau mice.

A. NMDA (40 μM) increases NO production in neurons dissociated from 2-3-month-old WT mice, but not in neurons from age-matched PS19 or rTg4510 mice. N=6/group; two-tailed paired t-test. ***B***. NMDA (100 μM)-induced NO production, detected amperometrically, is attenuated in PS19 mice compared to WT. N=5/group; two-tailed unpaired t-test. ***C***. Recombinant tau (rTau; P301L mutant; 400 nM) attenuates NO production induced by NMDA in WT neurons. N=7/group; one-way ANOVA and Tukey's test. ***D***. Total tau and phosphorylated tau (pTau) are elevated in post-synaptic density (PSD) preparations from 2-3-month-old PS19 (PS) compared to age-matched WT mice. N=12 for WT total Tau, pTau (AT8), and pTau (PHF13); N=13 for PS total tau; N=7 for PS pTau (AT8); N=5 for PS pTau (PHF13); two-tailed unpaired t-test. Data are presented as mean±SEM. ***E***. The association of GluN2B to PSD95, detected by co-immunoprecipitation (IP), is comparable in PS19 and WT mice. N=6/group. Data are presented as mean±SEM. ***F***. Association of PSD95 with nNOS, assessed by IP, is markedly reduced in PS19 mice compared to WT. Data are

presented as mean±SEM. N=8/group; two-tailed unpaired t-test. Immunoblots in ***D, E,*** and F are cropped; full gel pictures are shown in Source Data 5

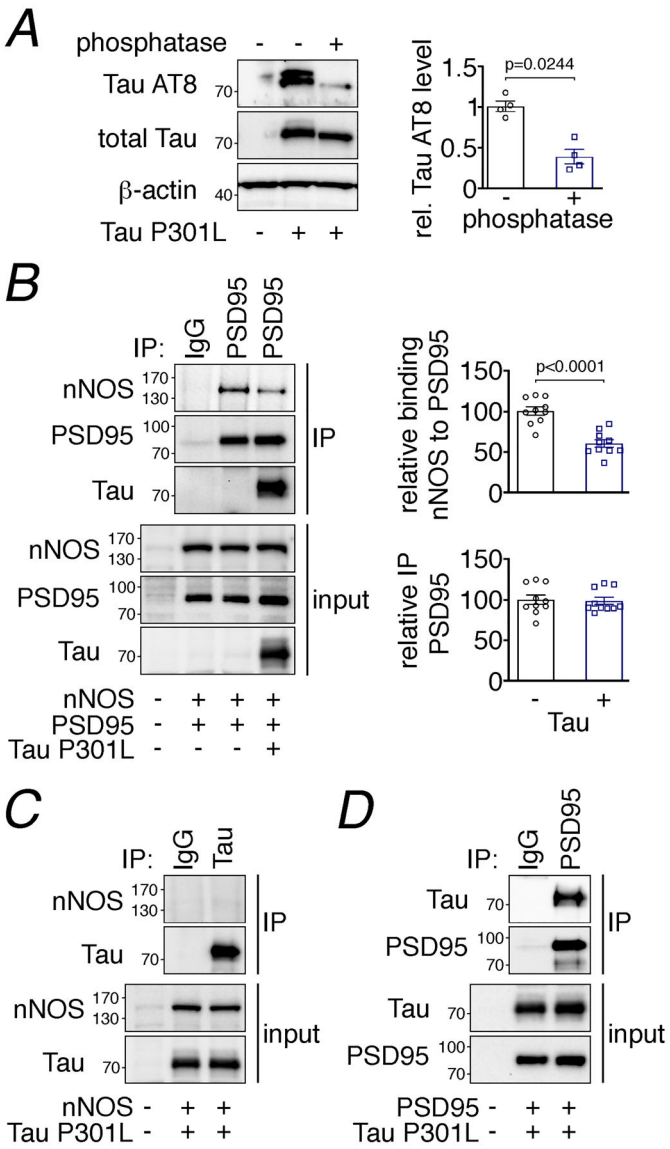

Figure 8: Tau disrupts PSD95-nNOS association by binding to PSD95.

A. Exogenously expressed Tau P301L in HEK293T cells is phosphorylated, as shown by sensitivity to phosphatase treatment. N=4/group; two-tailed paired t-test. Data are presented as mean±SEM. ***B.*** Co-expression of Tau P301L reduces PSD95 association with nNOS. PSD95 was immunoprecipitated (IP) and associated nNOS was detected. N=10/group; two-tailed unpaired t-test. Data are presented as mean±SEM. ***C.*** nNOS does not bind to immunoprecipitated Tau P301L. A representative blot is shown from N=9/group. ***D.*** Tau P301L associates with PSD95, which was immunoprecipitated (IP) from HEK293T cell lysates. Data are presented as mean±SEM. A representative image is shown from N=9/group. Immunoblots in are cropped; full gel pictures are shown in Source Data 6